



HATS-43b, HATS-44b, HATS-45b, and HATS-46b: Four Short-period Transiting Giant Planets in the Neptune–Jupiter Mass Range*

R. Brahm^{1,2}, J. D. Hartman³, A. Jordán^{1,2,4}, G. Á. Bakos^{3,17,18}, N. Espinoza^{1,2}, M. Rabus^{2,4}, W. Bhatti³, K. Penev³, P. Sarkis^{4,5}, V. Suc², Z. Csubry³, D. Bayliss⁶, J. Bento⁷, G. Zhou⁸, L. Mancini^{4,9,10}, T. Henning⁴, S. Ciceri¹¹, M. de Val-Borro³, S. Shectman¹², J. D. Crane¹², P. Arriagada¹³, P. Butler¹³, J. Teske^{12,13}, I. Thompson¹², D. Osip¹⁴, M. Díaz¹⁵, B. Schmidt⁷, J. Lázár¹⁶, I. Papp¹⁶, and P. Sári¹⁶

¹ Millennium Institute of Astrophysics, Santiago, Chile; rbrahm@astro.puc.cl

² Instituto de Astrofísica, Facultad de Física, Pontificia Universidad Católica de Chile, Av. Vicuña Mackenna 4860, 7820436 Macul, Santiago, Chile

³ Department of Astrophysical Sciences, Princeton University, NJ 08544, USA

⁴ Max-Planck-Institut für Astronomie, Königstuhl 17, D-69117 Heidelberg, Germany

⁵ Physikalisches Institut, Universität Bern, Gesellschaftstrasse 6, 3012 Bern, Switzerland

⁶ Observatoire Astronomique de l'Université de Genève, 51 ch. des Maillettes, 1290 Versoix, Switzerland

⁷ Research School of Astronomy and Astrophysics, Australian National University, Canberra, ACT 2611, Australia

⁸ Harvard-Smithsonian Center for Astrophysics, 60 Garden Street, Cambridge, MA 02138, USA

⁹ Dipartimento di Fisica, Università di Roma Tor Vergata, Via della Ricerca Scientifica 1, I-00133 Roma, Italy

¹⁰ INAF—Osservatorio Astrofisico di Torino, Via Osservatorio 20, I-10025—Pino Torinese, Italy

¹¹ Department of Astronomy, Stockholm University, SE-11419, Stockholm, Sweden

¹² The Observatories of the Carnegie Institution for Science, 813 Santa Barbara Street, Pasadena, CA 91101, USA

¹³ Department of Terrestrial Magnetism, The Carnegie Institution for Science, NW Washington, DC 20015-1305, USA

¹⁴ Las Campanas Observatory, The Carnegie Institution for Science, Colina el Pino, Casilla 601 La Serena, Chile

¹⁵ Departamento de Astronomía, Universidad de Chile, Camino el Observatorio 1515, Casilla 36-D, Las Condes, Santiago, Chile

¹⁶ Hungarian Astronomical Association, 1451 Budapest, Hungary

Received 2017 July 21; revised 2017 December 21; accepted 2018 January 5; published 2018 February 14

Abstract

We report the discovery of four short-period extrasolar planets transiting moderately bright stars from photometric measurements of the HATSouth network coupled to additional spectroscopic and photometric follow-up observations. While the planet masses range from 0.26 to 0.90 M_J , the radii are all approximately a Jupiter radii, resulting in a wide range of bulk densities. The orbital period of the planets ranges from 2.7 days to 4.7 days, with HATS-43b having an orbit that appears to be marginally non-circular ($e = 0.173 \pm 0.089$). HATS-44 is notable for having a high metallicity ($[Fe/H] = 0.320 \pm 0.071$). The host stars spectral types range from late F to early K, and all of them are moderately bright ($13.3 < V < 14.4$), allowing the execution of future detailed follow-up observations. HATS-43b and HATS-46b, with expected transmission signals of 2350 ppm and 1500 ppm, respectively, are particularly well suited targets for atmospheric characterization via transmission spectroscopy.

Key words: planetary systems – stars: individual (HATS-43, HATS-44, HATS-45, HATS-46)

Supporting material: machine-readable table

1. Introduction

By measuring their masses and radii, transiting planets orbiting moderately bright stars offer the unique opportunity to study in depth the physical structure of planets other than those present in the solar system. This property makes transiting planets one of the most valuable resources for testing current models of planet formation and evolution (e.g., Mordasini et al. 2012). In addition, detailed follow-up observations of these systems allowed us to study the structure and composition of their atmospheres (e.g., Fraine

et al. 2014) and to refine their orbital configuration and evolution by measuring the misalignment angle between the orbit and the spin axis of their host stars (e.g., Zhou et al. 2015).

Ground-based photometric surveys like HATNet (Bakos et al. 2004) and SuperWASP (Pollacco et al. 2006) have been a key and cost-efficient resource in contributing to the current number of ~ 300 discovered transiting systems with masses and radii determined with a precision better than 30%. Even though the population of discovered systems is highly biased toward the detection of giant planets at short distances from their stars (hot Jupiters), the increase of discoveries in this region of the parameter space has been fundamental for achieving statistically significant results that are helping to solve some of the theoretical challenges present in the field. For example, Hartman et al. (2016), using the full population of well characterized transiting systems, found that the radii of close-in planets increase as the parent stars evolve. This fact supports the theories that propose that hot Jupiters are inflated due to energy deposited deep into the planet interior (e.g., Batygin & Stevenson 2010) and not due to a delayed cooling (Burrows et al. 2007).

* The HATSouth network is operated by a collaboration consisting of Princeton University (PU), the Max Planck Institute für Astronomie (MPIA), the Australian National University (ANU), and the Pontificia Universidad Católica de Chile (PUC). The station at Las Campanas Observatory (LCO) of the Carnegie Institution is operated by PU in conjunction with PUC, the station at the High Energy Spectroscopic Survey (H.E.S.S.) site is operated in conjunction with MPIA, and the station at Siding Spring Observatory (SSO) is operated jointly with ANU. This paper includes data gathered with the MPG 2.2 m and ESO 3.6 m telescopes at the ESO Observatory in La Silla. This paper includes data gathered with the 6.5 meter *Magellan* Telescopes located at Las Campanas Observatory, Chile.

¹⁷ Alfred P. Sloan Research Fellow.

¹⁸ Packard Fellow.

Despite the importance of continuing the discovery of short-period gas giants, most of the efforts of the community are being put into the detection of well characterized transiting planets located in sparsely populated regions of the parameter space. Planets with periods longer than 10 days and/or sub-Saturn-mass planets are particularly interesting. While these types of planets are among the prime discovery targets of the ongoing *Kepler* K2 mission (Howell et al. 2014), and will be also efficiently discovered by TESS (Ricker et al. 2014), several new ground-based photometric surveys were designed to dig into these planetary regimes. Specifically, the HATSouth survey (Bakos et al. 2013), having three stations in three well separated locations in the southern hemisphere, has an increased efficiency for detecting both longer-period giant planets (warm Jupiters), and planets within the Neptune–Saturn-mass range, if compared to typical single site surveys (e.g., Bakos et al. 2015; Bayliss et al. 2015; Brahm et al. 2016).

In this paper, we present the discovery of four new well characterized short-period transiting planets from the HATSouth survey. In Section 2, we summarize the detection of the photometric planetary signal, and spectroscopic and photometric follow-up observations. In Section 3, we describe the analysis that was carried out in order to rule out false positives and to derive the parameters of the planets and host stars. Finally, in Section 4, we summarize the properties of each system and we discuss our findings in the context of the full population of discovered transiting systems.

2. Observations

2.1. Photometric Detection

The discovery of the periodic planetary-like photometric signals for the four systems presented in this study were obtained from the images registered by the three stations of the HATSouth network (the HS1 and HS2 instruments in Chile, HS3 and HS4 in Namibia, and HS5 and HS6 in Australia). Observations were performed with a typical cadence of 5 minutes using a Sloan *r* photometric filter. The specific properties of the observations that allowed the discovery of the planets are summarized in Table 1. As can be noticed in this table, the total number of images obtained per station varies from 700 to 9000 images, and were strongly dependent on the weather conditions and technical issues present on each site. In addition, the number of images obtained for different objects also depends on the adopted observing strategy and the position of the target in the field, because targets located in the edges of fields are usually also monitored when observing contiguous fields, as is the case in this work for HATS-44 and HATS-46.

The original images were reduced to photometric light curves by following the procedures described in Penev et al. (2013). The light curves thus generated were corrected for systematic signals using the Trend Filtering Algorithm (TFA; Kovács et al. 2005) and then the Box Least Squares (BLS; Kovács et al. 2002) method was applied to identify periodic transit-like features on them. Figure 1 shows the phase-folded light curves for the four systems analyzed in this study, which presented periodic dimmings in their fluxes with depths (10–30 mmag) and durations (1.6–3.2 hr) compatible with being short-period transiting giant planets. Due to these properties, these systems were added to the HATSouth database of planetary candidates. HATS-43b was observed during transit in 14 individual events. Each event was

composed of between 2 and 29 individual data points. For HATS-44b, on the other hand, we were able to observe 58 transit events, each one composed of between 1 and 18 data points. HATS-45b was observed in transit by the HATSouth automated units in 15 distinct events, with between 2 and 32 points per event. Finally, 33 transit events were observed for HATS-46b, and between 2 and 53 data points were obtained in each event. The light curve data for these four systems are presented in Table 7, at the end of the paper.

2.2. Spectroscopic Observations

To confirm the planetary nature of the candidates discovered by the HATSouth network, they are subject of an extensive follow-up campaign that involves the use of different facilities containing spectroscopic instruments with a wide range of capabilities. All of the spectrographs used for the discovery of the four HATS planets presented in this work are listed in Table 2 along with the general properties of the observations.

2.2.1. Reconnaissance Spectroscopy

After the initial photometric detection, the four candidates presented in the previous section were first observed with the WiFeS spectrograph (Dopita et al. 2007) installed at the ANU 2.3 m telescope. As described in Bayliss et al. (2013), observations are performed with two instrument configurations. A single $R = 3000$ spectra is obtained for each candidate in order to perform a spectral classification of the star by determining its effective temperature (T_{eff}), surface gravity ($\log g$), and metallicity ($[\text{Fe}/\text{H}]$) by using a library of synthetic spectra. The principal goal of this procedure is the identification of giant stars for which the observed transit depth could not be produced by planetary companions. In this way, HATS-43 and HATS-44 were identified as K-dwarfs with $T_{\text{eff}} = 4900 \pm 300$ K, $\log g = 5.0 \pm 0.3$ dex, and $T_{\text{eff}} = 4750 \pm 300$ K, $\log g = 4.3 \pm 0.3$ dex, respectively, while HATS-45 and HATS-46 were typed as an F-dwarf (6250 ± 300 K, 3.7 ± 0.3) and a G-dwarf (5800 ± 300 K, 4.5 ± 0.3), respectively. Additionally, multiple spectra for each candidate are obtained with a resolving power of $R = 7000$, with the goal of measuring radial velocity (RV) variations with a precision of $\sim 2 \text{ km s}^{-1}$ for identifying systems in which the transit-like signal is produced by stellar mass companions. The number of velocity points obtained for each candidate were 2, 4, 3, and 3 for HATS-43-44-45 and -46, respectively, and they were focused on phases ~ 0.25 and ~ 0.75 where the maximum velocity difference is expected. No significant velocity variations at the level of $\sim 4 \text{ km s}^{-1}$ were observed for any of the four candidates.

The lack of high-amplitude velocity variations and the dwarf status of the host stars for the four HATS candidates provided the first evidences in favor of the planetary origin of the photometric signals described in Section 2.1

2.2.2. Precision Radial Velocities

Precision radial velocities are required to confirm the planetary nature of a transiting companion by providing the means to estimate its mass and orbital parameters. For this purpose, we used the FEROS spectrograph (Kaufer & Pasquini 1998) installed at the MPG 2.2 m telescope. The high efficiency of this instrument coupled with its high resolving power of $R = 50,000$ allows us to achieve a long-term radial

Table 1
Summary of Photometric Observations

Instrument/Field ^a	Date(s)	# Images	Cadence ^b (second)	Filter	Precision ^c (mmag)
HATS-43					
HS-2.4/G598	2013 Sep–2014 Mar	739	285	<i>r</i>	13.4
HS-4.4/G598	2013 Sep–2014 Feb	4154	345	<i>r</i>	11.4
HS-6.4/G598	2013 Sep–2014 Mar	3865	357	<i>r</i>	10.9
1 m+CTIO/SBIG	2016 Aug 21	44	219	<i>i</i>	1.3
LCOGT 1 m+CTIO/sinistro	2016 Oct 26	69	219	<i>i</i>	1.1
HATS-44					
HS-2.3/G598	2013 Sep–2014 Mar	745	285	<i>r</i>	12.4
HS-4.3/G598	2013 Sep–2014 Feb	4143	345	<i>r</i>	13.5
HS-6.3/G598	2013 Sep–2014 Mar	3836	357	<i>r</i>	13.3
HS-1.2/G599	2012 Jan–2013 Apr	9325	292	<i>r</i>	12.1
HS-3.2/G599	2012 Jan–2013 Apr	3174	288	<i>r</i>	12.9
HS-5.2/G599	2012 Jan–2013 Apr	5004	288	<i>r</i>	12.7
1 m+SAAO/SBIG	2015 Nov 07	63	194	<i>i</i>	2.2
LCOGT 1 m+CTIO/sinistro	2015 Nov 15	55	219	<i>i</i>	5.4
LCOGT 1 m+CTIO/SBIG	2015 Nov 26	41	194	<i>g</i>	6.9
HATS-45					
HS-2.2/G554	2009 Dec–2011 May	6414	296	<i>r</i>	8.0
HS-4.2/G554	2009 Dec–2011 Mar	953	383	<i>r</i>	10.2
HS-6.2/G554	2010 Dec–2011 May	2097	300	<i>r</i>	8.5
Swope 1 m/e2v	2014 Mar 22	81	160	<i>i</i>	1.6
CTIO 0.9 m	2014 Oct 13	36	181	<i>i</i>	1.9
LCOGT 1 m+SAAO/SBIG	2015 Mar 09	25	200	<i>i</i>	1.4
LCOGT 1 m+CTIO/sinistro	2015 Mar 14	51	226	<i>i</i>	1.5
HATS-46					
HS-2.3/G754	2012 Sep–2012 Dec	3875	282	<i>r</i>	9.2
HS-4.3/G754	2012 Sep–2013 Jan	3191	292	<i>r</i>	9.9
HS-6.3/G754	2012 Sep–2012 Dec	2994	285	<i>r</i>	9.7
HS-1.2/G755	2011 Jul–2012 Oct	5265	292	<i>r</i>	9.6
HS-3.2/G755	2011 Jul–2012 Oct	4851	287	<i>r</i>	10.3
HS-5.2/G755	2011 Jul–2012 Oct	6018	296	<i>r</i>	9.3
Swope 1 m/e2v	2014 Nov 30	64	169	<i>i</i>	1.7
LCOGT 1 m+CTIO/sinistro	2016 Aug 31	55	219	<i>i</i>	1.1

Notes.

^a For HATSouth data, we list the HATSouth unit, CCD, and field name from which the observations are taken. HS-1 and –2 are located at Las Campanas Observatory in Chile, HS-3 and –4 are located at the H.E.S.S. site in Namibia, and HS-5 and –6 are located at Siding Spring Observatory in Australia. Each unit has 4 ccds. Each field corresponds to one of 838 fixed pointings used to cover the full 4π celestial sphere. All data from a given HATSouth field and CCD number are reduced together, while detrending through External Parameter Decorrelation (EPD) is done independently for each unique unit+CCD+field combination.

^b The median time between consecutive images rounded to the nearest second. Due to factors such as weather, the day–night cycle, guiding and focus corrections the cadence is only approximately uniform over short timescales.

^c The rms of the residuals from the best-fit model.

velocity precision in the range of $10\text{--}50\text{ ms}^{-1}$ for our $V > 13$ candidates by obtaining spectra with ~ 1800 s of exposure time using the simultaneous wavelength calibration technique (Baranne et al. 1996). In the case of HATS-43, –44, and –45, we obtained on the order of 15 FEROS spectra, while for HATS-46, 31 FEROS spectra were acquired. All FEROS spectra were reduced, extracted and analyzed using the CERES pipeline (Brahm et al. 2017a). The images are processed using an optimal extraction algorithm, and then each spectrum is wavelength calibrated and corrected by instrumental drifts. Radial velocities are determined with the cross-correlation technique where a G2-like binary mask is used as template. Bisector spans are also measured for each spectrum by CERES.

Figure 3 shows that the FEROS velocities obtained for the four systems have a time correlated variation, which is in phase with the photometric ephemerides and has an amplitude consistent with planetary-mass objects. However, only in the case of HATS-44, the FEROS velocities were enough for measuring the semi-amplitude with a precision better than 25% ($K = 90 \pm 17\text{ ms}^{-1}$). For the remaining candidates, additional observations were required as we now describe.

HATS-43 and HATS-45 were observed with the HARPS instrument (Mayor et al. 2003) mounted on the ESO 3.6 m telescope, which is located at the ESO La Silla Observatory. Observations were performed with the Object+Sky mode because the daily internal drifts of the instrument are smaller

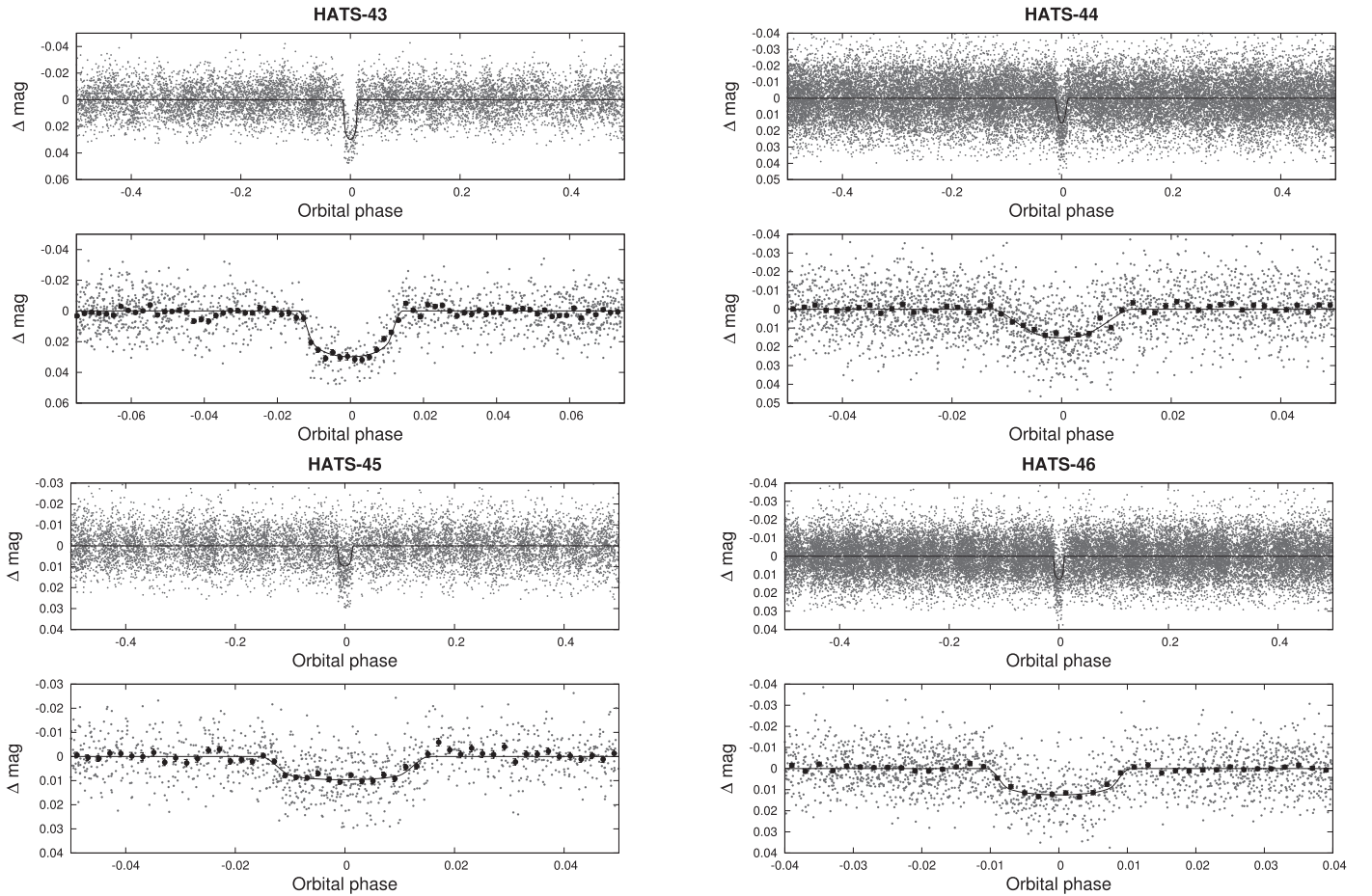


Figure 1. Phase-folded unbinned HATSouth light curves for HATS-43 (upper left), HATS-44 (upper right), HATS-45 (lower left), and HATS-46 (lower right). In each case, we show two panels. The top panel shows the full light curve, while the bottom panel shows the light curve zoomed-in on the transit. The solid lines show the model fits to the light curves. The dark filled circles in the bottom panels show the light curves binned in phase with a bin size of 0.002.

than 1 ms^{-1} , which is significantly smaller than the radial velocity precision that we require. HARPS data was also reduced and analyzed with CERES. By using these additional velocities, the semi-amplitudes of the orbits for HATS-43 and HATS-45 were determined with a precision better than 25%. While the combined RVs for HATS-45 suggest that the star is orbited by a typical hot-Jupiter, the velocities for HATS-43 are consistent with the presence of a Saturn-mass planet with a non-negligible eccentricity. For these two planets, we also obtained a single spectrum using the Coralie Spectrograph mounted on the 1.2 m Euler telescope installed at the ESO La Silla Observatory. Both spectra were processed with CERES but were not used in the analysis because no velocity variations could be computed from a single radial velocity epoch.

Finally, HATS-46 was observed with the Planet Finder Spectrograph (PFS; Crane et al. 2010) mounted on the *Magellan*/Clay 6.5 m telescope at Las Campanas Observatory. As has been described in previous HATSouth discoveries (Jordán et al. 2014; Zhou et al. 2014; Hartman et al. 2015), we obtained a template spectrum by using the $0''.5$ slit, which was then used as reference for computing the radial velocities at different epochs by obtaining spectra with an I2-cell. The 11 spectra that were acquired with the I2-cell were processed as described in Butler et al. (1996). The mean RV precision achieved was $\sim 20 \text{ ms}^{-1}$ and was principally limited by the faintness of the star. By combining the velocities measured by FEROS and PFS for HATS-46 we were able to confirm the

planetary nature of this candidate and infer for it a sub-Saturn-mass.

The radial velocities and bisector spans obtained with FEROS, Coralie, and HARPS for the four discovered planets are presented in Table 6 at the end of the paper. We investigated if there is a significant degree of correlation between the radial velocities and the bisector span measurements that could suggest that the observed velocity variations are produced by a blended stellar companion. Specifically, we followed the procedure adopted in Bhatti et al. (2016) and for each of our four systems, we computed the error weighted distribution for the Pearson correlation coefficient by applying a bootstrap method. The derived 95% confidence intervals for the correlation coefficient are $[-0.57, 0.30]$, $[-0.59, 0.02]$, $[-0.35, 0.46]$, and $[-0.22, 0.65]$, for HATS-43, HATS-44, HATS-45, and HATS-46, respectively, implying that there is no significant correlation and thus supporting the planetary hypothesis as the cause of the observed velocity variations. Figure 2 shows the radial velocities versus bisector spans diagrams for each of the four systems.

2.3. Photometric Follow-up Observations

In addition to the HATSouth discovery light curves, we observed transits for the four discovered planets using telescopes with larger apertures in order to: (i) confirm that the photometric signals are real, (ii) refine the ephemerides of

Table 2
Summary of Spectroscopy Observations

Instrument	UT Date(s)	# Spec.	Res. $\Delta\lambda/\lambda/1000$	S/N Range ^a	γ_{RV}^b (km s ⁻¹)	RV Precision ^c (m s ⁻¹)
HATS-43						
ANU 2.3 m/WiFeS	2015 Feb 6	1	3	68
ANU 2.3 m/WiFeS	2015 Feb 6–8	2	7	57–82	23.2	4000
MPG 2.2 m/FEROS	2015 Oct–2016 Dec ^d	12	48	15–50	22.078	25
ESO 3.6 m/HARPS	2016 Apr–Nov	7	115	10–24	22.053	24
Euler 1.2 m/Coralie ^d	2016 Aug 10	1	60	12	22.002	...
HATS-44						
ANU 2.3 m/WiFeS	2015 Jan 1	1	3	54
ANU 2.3 m/WiFeS	2015 Jan–Aug	4	7	50–101	47.4	4000
MPG 2.2 m/FEROS	2015 Oct–2016 Dec	15	48	19–36	44.082	50
HATS-45						
ANU 2.3 m/WiFeS	2013 Sep 27	1	3	87
ANU 2.3 m/WiFeS	2014 Feb 17–23	3	7	44–70	20.8	4000
Euler 1.2 m/Coralie ^d	2014 Sep 12	1	60	12	19.19	...
MPG 2.2 m/FEROS ^d	2015 Jan–2016 Feb	13	48	22–70	19.423	50
ESO 3.6 m/HARPS	2015 Feb 14–19	6	115	14–24	19.372	28
HATS-46						
ANU 2.3 m/WiFeS	2014 Oct 4	1	3	64
ANU 2.3 m/WiFeS	2014 Oct 4–7	3	7	36–80	–30.5	4000
MPG 2.2 m/FEROS ^d	2015 Jun–2016 Dec	31	48	16–57	–30.193	35
Magellan 6.5 m/PFS+I ₂	2015 Jun–2016 Dec	11	76	45–55	...	24
Magellan 6.5 m/PFS	2015 Jun	3	76	59–61

Notes.

^a S/N per resolution element near 5180 Å.

^b For high-precision RV observations included in the orbit determination, this is the zero-point RV from the best-fit orbit. For other instruments, it is the mean value. We do not provide this quantity for the lower resolution WiFeS observations, which were only used to measure stellar atmospheric parameters.

^c For high-precision RV observations included in the orbit determination, this is the scatter in the RV residuals from the best-fit orbit (which may include astrophysical jitter), for other instruments, this is either an estimate of the precision (not including jitter), or the measured standard deviation. We do not provide this quantity for low-resolution observations from the ANU 2.3 m/WiFeS.

^d We excluded from the analysis the single Coralie observations of HATS-43 and HATS-45. We also excluded from the analysis one FEROS observation of HATS-43 obtained on UT 2015 October 30, and one FEROS observation of HATS-45 obtained on UT 2015 February 2, both of which were affected by significant sky contamination. For HATS-46, which has a very low amplitude RV orbital wobble, and for which even slight sky contamination can obscure the signal, we excluded 11 FEROS observations due to evidence of sky contamination as seen in the computed CCFs. The excluded observations are from UT 2015 June 10, and 21, July 20, October 2, 4, 26, 27 and 30, and November 3, and 2016 July 26 and September 14.

the systems, and (iii) measure the transiting parameters with a higher precision; an accurate determination of R_p/R_* and a/R_* is particularly important for obtaining a reliable estimation of the planetary physical parameters. The basic configurations used in these observations are listed in Table 1, while the light curve data is presented in Table 7.

As shown in Figure 4, an ingress and an almost full transit including a complete egress of HATS-43b were observed using the 1 m telescope of the Las Cumbres Observatory Global Telescope (LCOGT) network (Brown et al. 2013) located at the Cerro Tololo International Observatory (CTIO). Both observations were performed during the second semester of 2016, approximately 3 years after the original HATSouth photometry was obtained. Even though both light curves were obtained with the Sloan *i* band, the one containing the egress was registered by a SBIG camera, while the full transit was registered using the Sinistro camera. In both cases, the per-point photometric precision was of ~ 1.5 mmag with a cadence of ≈ 219 s.

Three full transits of HATS-44b were observed in 2015 November using the LCOGT 1 m network (see Figure 5). The

first one was obtained from the South African Astronomical Observatory (SAAO) using the Sloan *i* filter and a SBIG camera, achieving a photometric precision of ≈ 2 mmag with a cadence of ≈ 200 s. The second transit was observed from CTIO with the same filter but using a Sinistro camera. The observing conditions were not optimal which resulted in the photometric precision being only ~ 5 mmag with a cadence of ≈ 200 s. The last transit was also observed from CTIO but this time the Sloan *g* band was used with the goal of checking that there was no color dependence of the transit depth such as would be produced by a blended eclipsing binary system, given the slightly triangular shape of this transit. Even though the precision obtained for this transit was relatively low (~ 7 mmag with a cadence of ≈ 200 s), it was enough to confirm that there was no significant variation in the transit depth between the *r* and *g* filters.

For HATS-45b we obtained four *i*-band follow-up light curves, which are shown in Figure 6. The first light curve was obtained in 2014 March and registered a full transit using the 1 m Swope telescope and e2v CCD camera. The second light curve was obtained on 2014 October using the 0.9 m Telescope

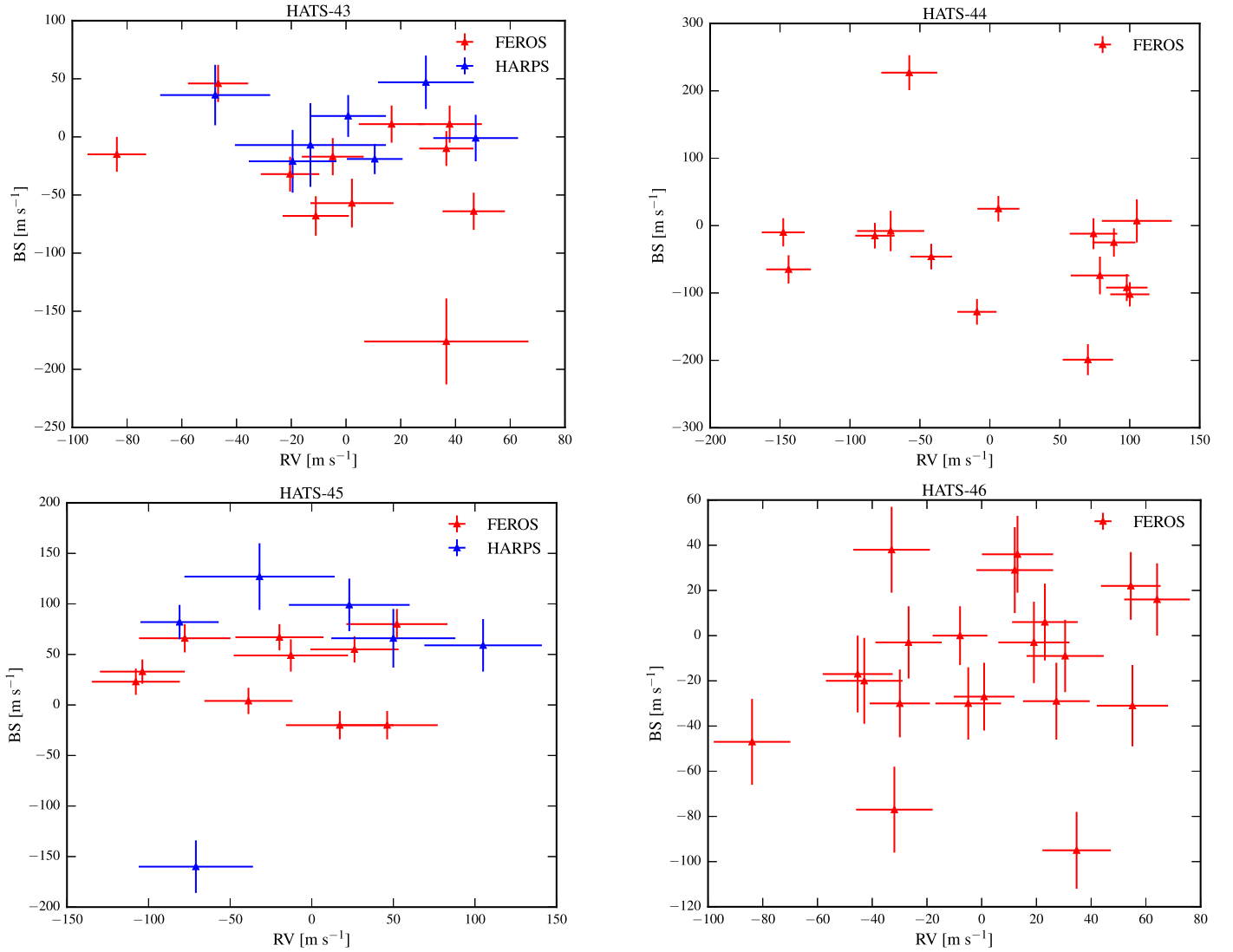


Figure 2. RV vs. bisector span measurements for HATS-43 (upper left), HATS-44 (upper right), HATS-45 (lower left), and HATS-46 (lower right). No significant correlation at the 95% level was identified, which indicates that the RV variations are probably produced by planetary-mass orbital companions.

of CTIO and registered only an egress. The last two light curves were obtained on 2015 March with the LCOGT 1 m network, with an ingress observed from SAAO and an egress from CTIO. The photometric precision for these four light curves was in the 1–2 mmag range with cadences ≈ 200 s.

Finally, two *i*-band transits were observed for HATS-46b, which are shown in Figure 7. In 2014 November, a partial transit containing an egress was observed with the Swope 1 m telescope, while in 2016 August, we registered a full transit with the LCOGT 1 m telescope installed at CTIO using a Sinistro camera. Both light curves achieved a photometric precision below 2 mmag at ≈ 200 s cadence.

The instrument specifications, observing strategies and reduction procedures that we apply in the case of the three instruments that were used to obtain photometry for our four planets have been previously discussed in Bayliss et al. (2015), Penev et al. (2013), and Hartman et al. (2015), for LCOGT, Swope 1 m, and CTIO 0.9 m, respectively.

2.4. High Spatial Resolution Imaging

As part of our follow-up campaign, we also obtain high-resolution “lucky” imaging for identifying close stellar

companions to our candidates. If present, these companions could be affecting the depth of the transits. In this context, HATS-45 was observed with the Astralux Sur camera (Hippler et al. 2009) mounted on the New Technology Telescope (NTT) at La Silla Observatory, in Chile on 2015 December 22, in the Sloan z' band. Instrument specifications, observing strategy, and reductions of Astralux data are described in Espinoza et al. (2016). The only change in this work is that we used the plate scale derived in Janson et al. (2017) of 15.2 mas/pixel. No evident companion can be identified in the neighborhood of HATS-45 at the achieved resolution limit of $\text{FWHM}_{\text{eff}} = 40 \pm 4.6$ mas, which is within the expected telescope diffraction limit of (~ 50 mas Hippler et al. 2009). Figure 8 presents the contrast curve generated from the HATS-45 Astralux observations.

3. Analysis

3.1. Properties of the Parent Star

An initial estimation of the atmospheric parameters (T_{eff} , $\log g$, $[\text{Fe}/\text{H}]$, and $v \sin i$) for the four host stars was computed using the Zonal Atmospheric Parameters Estimator (ZASPE; Brahm

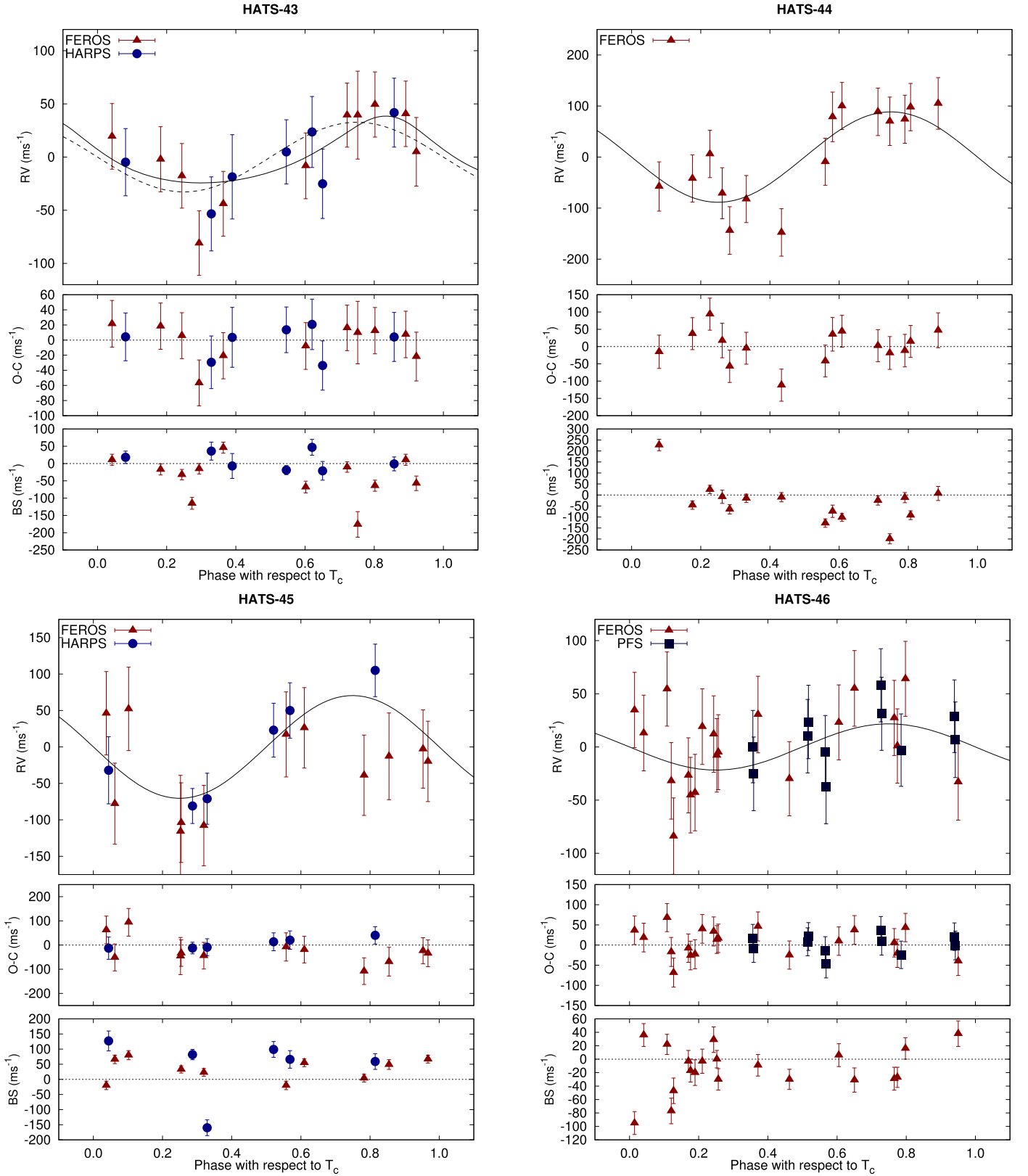


Figure 3. Phased high-precision RV measurements for HATS-43 (upper left), HATS-44 (upper right), HATS-45 (lower left), and HATS-46 (lower right). The instruments used are labeled in the plots. In each case, we show three panels. The top panel shows the phased measurements together with our best-fit model (see Table 4) for each system. Zero-phase corresponds to the time of mid transit. The center-of-mass velocity has been subtracted. For HATS-43, the circular fit is shown as a dashed line, while the eccentric (adopted) fit is represented as a solid line. The second panel shows the velocity $O - C$ residuals from the best fit. The error bars include the jitter terms listed in Table 4 added in quadrature to the formal errors for each instrument. The third panel shows the bisector spans (BS). Note the different vertical scales of the panels.

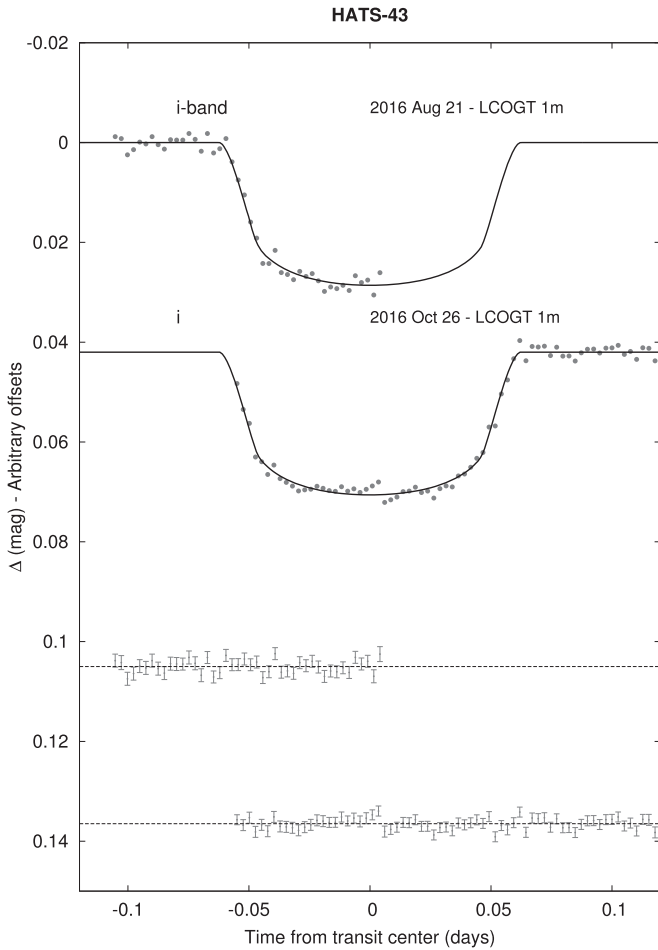


Figure 4. Unbinned transit light curves for HATS-43. The light curves have been corrected for quadratic trends in time, and linear trends with up to three parameters characterizing the shape of the PSF, fitted simultaneously with the transit model. The dates of the events, filters, and instruments used are indicated. Light curves following the first are displaced vertically for clarity. Our best fit from the global modeling described in Section 3.3 is shown by the solid lines. The residuals from the best-fit model are shown below in the same order as the original light curves. The error bars represent the photon and background shot noise, plus the readout noise.

et al. 2017b) applied to the FEROS follow-up spectra presented in Section 2.2. Due to the moderately low signal-to-noise ratio (S/N) of each individual spectrum, they were shifted to a common rest frame and co-added to construct a spectral template with $S/N \approx 50$ for each star. ZASPE determines the atmospheric parameters by comparing the observed spectra with a grid of synthetic models in the spectral regions most sensitive to changes in the parameters. Additionally, reliable errors are obtained by performing Monte Carlo simulations where the synthetic models are randomly modified in the sensitive regions by values obtained from the systematic mismatch between the observed spectra and the best-fit model.

To determine the physical and evolutionary parameters of the host star (M_* , R_* , age), we use the Yonsei–Yale (Y2; Yi et al. 2001) stellar isochrones to search for the mass and age of the model that produces the temperature and luminosity indicators closest to the observed ones. While the spectroscopic T_{eff} determined with ZASPE can be used as a direct temperature indicator, the uncertainty in the spectroscopic $\log g$ is usually too large to use this parameter as a reliable luminosity tracer. As is a common procedure now, the stellar luminosity indicator

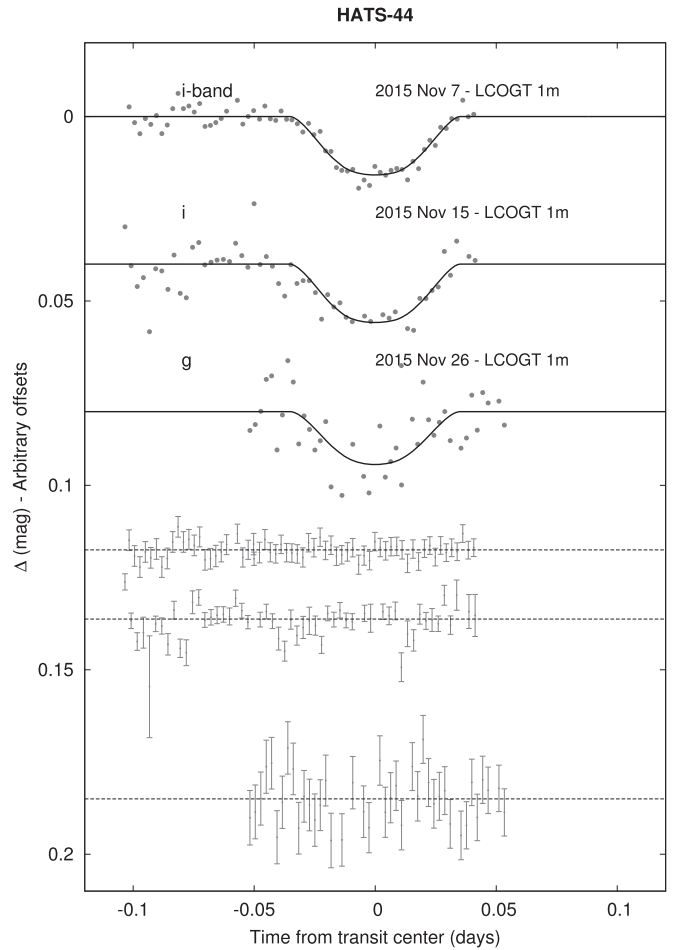


Figure 5. Similar to Figure 4, here we show light curves for HATS-44. In this case, the residuals are plotted on the lower part of the figure, in the same order as the original light curves on upper part.

is obtained from the transiting light curve, via the parameter a/R_* , which as described in Section 3.3 is directly related to the stellar density (Sozzetti et al. 2007). However, given that the modeling of the transiting light curve partially depends of the stellar parameters by the selection of the Claret (2004) limb-darkening coefficients, we follow an iterative procedure containing the following steps: (i) determination of the ZASPE parameters, (ii) global modeling (Section 3.3), and (iii) isochronal fitting. For the four transiting systems presented in this study, only two iterations were required.

Table 3 presents the final atmospheric and physical parameters adopted for the four host stars, while Figure 9 displays their evolutionary states in the $T_{\text{eff}}-\rho_*$ space, along with a set of different YY isochrones for the specific spectroscopically derived metallicities. All four stars are currently on the main sequence. HATS-43 and HATS-44 have relatively low masses of $M_* \approx 0.85 M_\odot$, characteristic of early K-dwarf stars. On the other hand, HATS-45, as expected from its higher spectroscopic derived $T_{\text{eff}} = 6450 \pm 110$ K, is a relatively massive star with an isochronal derived mass of $M_* = 1.272 \pm 0.048 M_\odot$. Finally, the derived properties of HATS-46 are similar, but slightly smaller than the ones of the Sun ($M_* = 0.917 \pm 0.027 M_\odot$, $R_* = 0.853^{+0.040}_{-0.030} R_\odot$). Only HATS-44, with $[\text{Fe}/\text{H}] = 0.320 \pm 0.071$, presents a significant deviation from solar metallicity.

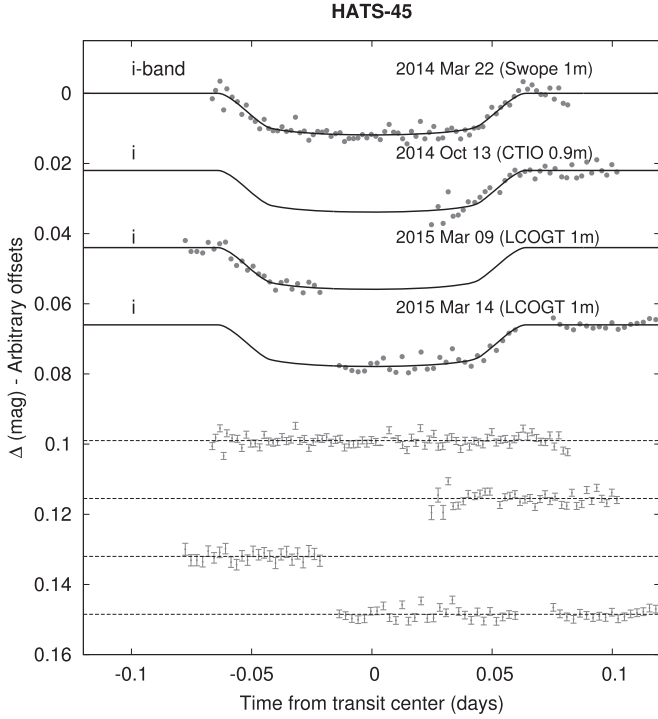


Figure 6. Similar to Figure 4, here we show one full and three partial follow-up light curves for HATS-45. The residuals are shown in the lower part of the figure.

3.2. Excluding Blend Scenarios

To exclude blend scenarios, we carried out an analysis following Hartman et al. (2012). We attempt to model the available photometric data (including light curves and catalog broad-band photometric measurements) for each object as a blend between an eclipsing binary star system and a third star along the line of sight. The physical properties of the stars are constrained using the Padova isochrones (Girardi et al. 2000), while we also require that the brightest of the three stars in the blend have atmospheric parameters consistent with those measured with ZASPE. We also simulate composite cross-correlation functions (CCFs) and use them to predict radial velocities and bisector spans for each blend scenario considered. The results for each system are as follows:

1. *HATS-43*—all blend scenarios tested provide a poorer fit to the photometric data than a model consisting of a single star with a planet. Based on this, all blend models can be rejected with at least 3σ confidence. Moreover, blend models that come closest to fitting the photometric data have obvious double peaks in their CCFs and would produce many km s^{-1} BS and RV variations that we do not detect.
2. *HATS-44*—similar to HATS-43, except here we can only reject blend models at 2.3σ confidence based on the photometry. The blend models that provide the best fit to the photometry (i.e., those that can be rejected with greater than 2.3σ confidence based on the photometry but that cannot be rejected with greater than 5σ confidence) have simulated RV measurements that do not resemble the observed sinusoidal RV variation. The best-fit blend model has $\Delta\chi^2 = 13.4$ compared to the adopted planetary orbit model, when including jitter in the uncertainties, and, based on an F-test, can be rejected

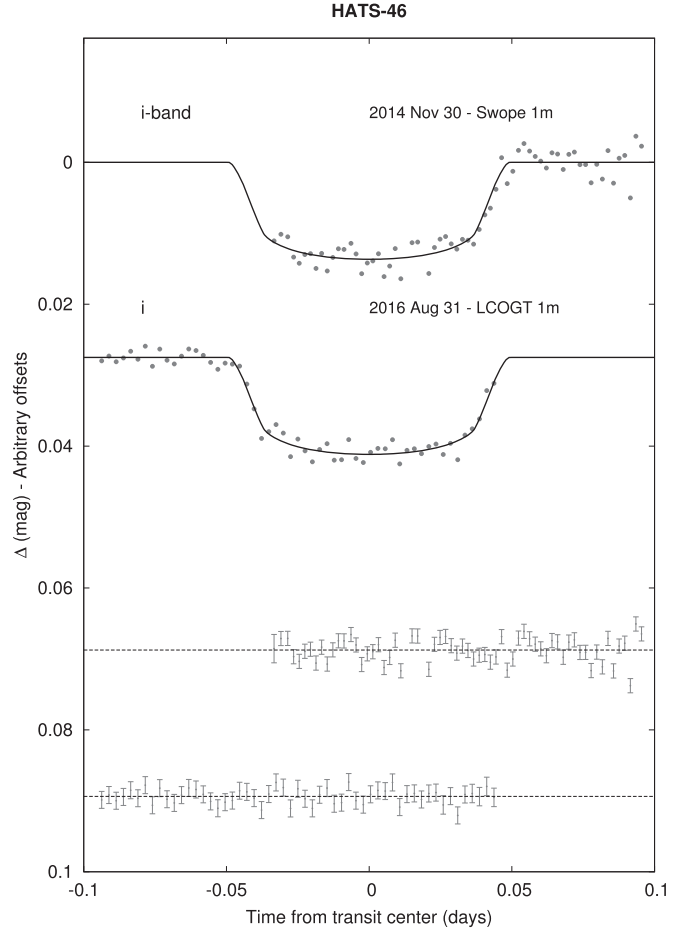


Figure 7. Here, we show two partial follow-up light curves for HATS-46 (upper part). The residuals of each light curve are presented in the lower part of the figure.

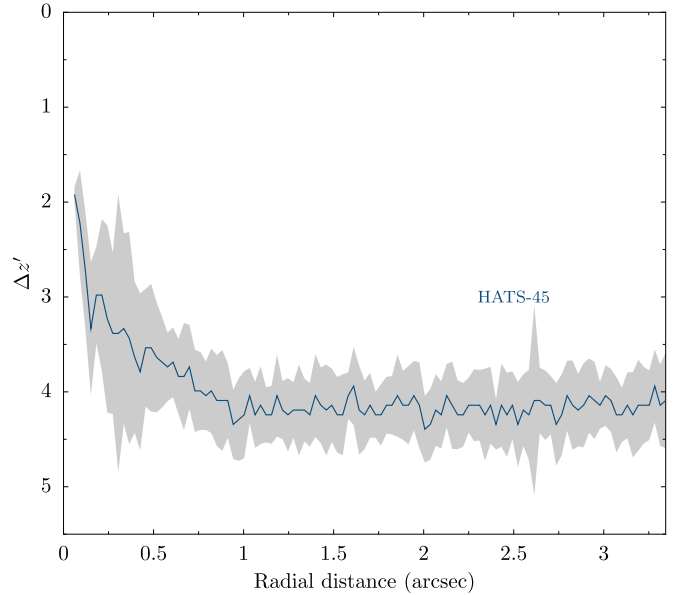


Figure 8. Contrast curve for HATS-45 constructed from the z' band Astralux images. Gray bands show the uncertainty given by the scatter in the contrast in the azimuthal direction at a given radius.

with 99.7% confidence. Combining the RVs and photometry, all blend models can be rejected with greater than 4σ confidence.

Table 3
Stellar Parameters for HATS-43–HATS-46

Parameter	HATS-43 Value	HATS-44 Value	HATS-45 Value	HATS-46 Value	Source
Astrometric properties and cross-identifications					
2MASS-ID	05220915-3058150	05371842-2758214	06475862-2154385	00264858-5618580	
GSC-ID	GSC 7048-01851	GSC 6497-00040	GSC 5961-02383	GSC 8468-01248	
R.A. (J2000)	05 ^h 22 ^m 09 ^s .16	05 ^h 37 ^m 18 ^s .41	06 ^h 47 ^m 58 ^s .63	00 ^h 26 ^m 48 ^s .58	2MASS
Decl. (J2000)	−30°58′15″.0	−27°58′21″.4	−21°54′38″.5	−56°18′58″.0	2MASS
$\mu_{R.A.}$ (mas yr ^{−1})	9.8 ± 1.9	−2.2 ± 1.3	−5.1 ± 2.5	21.3 ± 1.7	UCAC4
$\mu_{Decl.}$ (mas yr ^{−1})	7.9 ± 1.7	−3.1 ± 1.6	2.8 ± 1.6	5.0 ± 1.9	UCAC4
Spectroscopic properties					
$T_{\text{eff},*}$ (K)	5099 ± 61	5080 ± 100	6450 ± 110	5495 ± 69	ZASPE ^a
[Fe/H]	0.050 ± 0.041	0.320 ± 0.071	0.020 ± 0.068	−0.060 ± 0.046	ZASPE
$v \sin i$ (km s ^{−1})	1.11 ± 0.82	0.5 ± 1.1	9.90 ± 0.40	0.90 ± 0.66	ZASPE
v_{mac} (km s ^{−1})	2.948 ± 0.093	2.92 ± 0.15	5.03	3.56 ± 0.10	Assumed
v_{mic} (km s ^{−1})	0.747 ± 0.030	0.737 ± 0.051	1.69	0.932 ± 0.033	Assumed
γ_{RV} (m s ^{−1})	22077.5 ± 8.3	44082 ± 14	19423 ± 17	−30192.7 ± 8.6	FEROS ^b
Photometric properties					
B (mag)	14.471 ± 0.050	15.487 ± 0.020	13.845 ± 0.020	14.421 ± 0.010	APASS ^c
V (mag)	13.593 ± 0.030	14.428 ± 0.010	13.307 ± 0.050	13.634 ± 0.050	APASS ^c
g (mag)	13.973 ± 0.030	14.933 ± 0.010	13.550 ± 0.020	14.018 ± 0.010	APASS ^c
r (mag)	13.301 ± 0.020	14.086 ± 0.010	13.201 ± 0.060	13.487 ± 0.020	APASS ^c
i (mag)	13.094 ± 0.070	13.794 ± 0.030	13.162 ± 0.040	13.45 ± 0.22	APASS ^c
J (mag)	12.064 ± 0.026	12.699 ± 0.023	12.364 ± 0.024	12.366 ± 0.024	2MASS
H (mag)	11.646 ± 0.022	12.234 ± 0.022	12.155 ± 0.024	11.993 ± 0.022	2MASS
K_s (mag)	11.556 ± 0.023	12.188 ± 0.030	12.137 ± 0.021	11.965 ± 0.024	2MASS
Derived properties					
M_* (M_{\odot})	0.837 ± 0.023	0.860 ± 0.021	1.272 ± 0.048	0.917 ± 0.027	YY+ ρ_* +ZASPE ^d
R_* (R_{\odot})	0.812 ± 0.032	0.847 ± 0.036	1.315 ± 0.064	0.853 ^{+0.040} _{−0.030}	YY+ ρ_* +ZASPE
$\log g_*$ (cgs)	4.539 ± 0.036	4.514 ± 0.036	4.305 ± 0.036	4.542 ± 0.038	YY+ ρ_* +ZASPE
ρ_* (g cm ^{−3}) ^e	1.96 ± 1.00	1.59 ^{+0.46} _{−0.28}	0.81 ^{+0.16} _{−0.11}	3.20 ± 0.72	Light curves
ρ_* (g cm ^{−3}) ^e	2.18 ^{+0.36} _{−0.20}	1.98 ± 0.25	0.79 ± 0.10	2.10 ^{+0.22} _{−0.29}	YY+Light curves+ZASPE
L_* (L_{\odot})	0.400 ± 0.046	0.400 ± 0.051	2.66 ± 0.36	0.589 ± 0.070	YY+ ρ_* +ZASPE
M_V (mag)	5.97 ± 0.14	6.01 ± 0.16	3.68 ± 0.16	5.47 ± 0.14	YY+ ρ_* +ZASPE
M_K (mag,ESO)	3.91 ± 0.10	3.85 ± 0.11	2.58 ± 0.11	3.704 ± 0.098	YY+ ρ_* +ZASPE
Age (Gyr)	8.6 ^{+3.0} _{−4.8}	9.7 ^{+2.4} _{−4.0}	1.52 ± 0.70	3.0 ^{+3.4} _{−2.1}	YY+ ρ_* +ZASPE
A_V (mag)	0.000 ± 0.018	0.095 ± 0.064	0.042 ^{+0.106} _{−0.042}	0.000 ± 0.013	YY+ ρ_* +ZASPE
Distance (pc)	341 ± 17	463 ± 23	818 ± 41	448 ± 22	YY+ ρ_* +ZASPE

Notes. For HATS-43, we adopt a model in which the eccentricity is allowed to vary. For the other three systems we adopt a model in which the orbit is assumed to be circular. See the discussion in Section 3.3.

^a ZASPE = Zonal Atmospheric Stellar Parameter Estimator routine for the analysis of high-resolution spectra (Brahm et al. 2017b), applied to the FEROS spectra of each system. These parameters rely primarily on ZASPE, but have a small dependence also on the iterative analysis incorporating the isochrone search and global modeling of the data.

^b The error on γ_{RV} is determined from the orbital fit to the RV measurements and does not include the systematic uncertainty in transforming the velocities to the IAU standard system. The velocities have not been corrected for gravitational redshifts.

^c From APASS DR6 for as listed in the UCAC 4 catalog (Zacharias et al. 2012).

^d YY+ ρ_* +ZASPE = Based on the YY isochrones (yi:2001), ρ_* as a luminosity indicator, and the ZASPE results.

^e In the case of ρ_* , we list two values. The first value is determined from the global fit to the light curves and RV data, without imposing a constraint that the parameters match the stellar evolution models. The second value results from restricting the posterior distribution to combinations of ρ_* + $T_{\text{eff},*}$ + [Fe/H] that match to a YY stellar model.

3. *HATS-45*—similar to HATS-43, except here we can only reject blend models at 1.4 σ confidence based on the photometry alone. However, for blend models that cannot be rejected with at least 5 σ confidence based on the photometry, both the simulated BSs and RVs vary by more than 500 m s^{−1}, and in most cases by well over 1 km s^{−1} (compared to the measured scatter of 36 m s^{−1} and 61 m s^{−1} for the FEROS BS and RV values—including the planetary signal—of this target, respectively, and compared to the measured scatter of 104 m s^{−1} and 73 m s^{−1} for the HARPS BS and RV values, respectively).
4. *HATS-46*—similar to HATS-43, in this case all blend models tested can be rejected with 2.4 σ confidence based

solely on the photometry. For blend models that cannot be rejected with at least 4 σ confidence based on the photometry, both the simulated BSs and RVs vary by more than 200 m s^{−1} (compared to the measured scatter of 35 m s^{−1} and 39 m s^{−1} for the FEROS BS and RV values of this target, respectively).

3.3. Global Modeling of the Data

In order to obtain the orbital and physical parameters of the planets, we simultaneously modeled for each system the HATSouth photometry, the follow-up photometry, and the

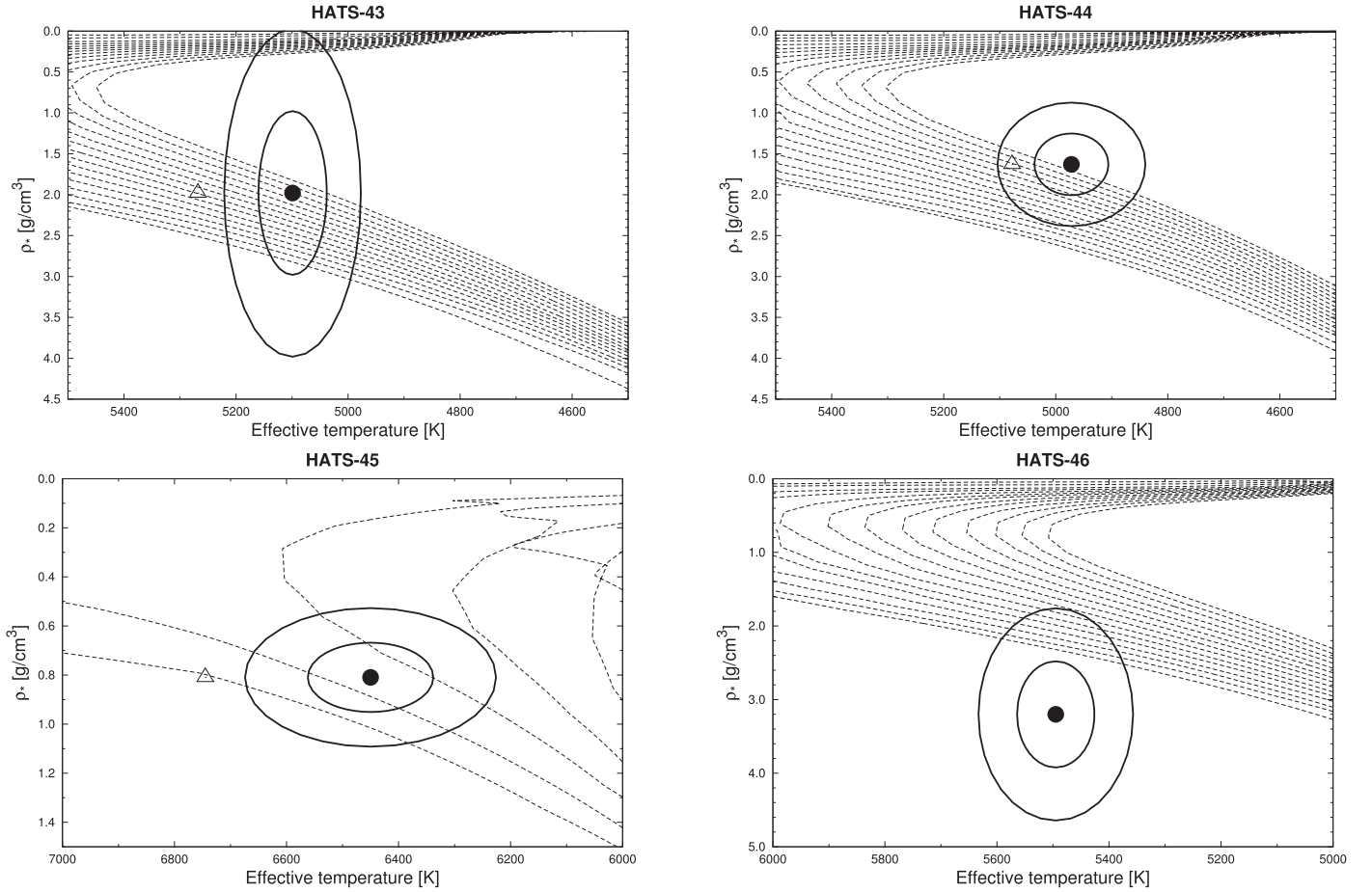


Figure 9. Model isochrones from Yi et al. (2001) for the measured metallicities of HATS-43 (upper left), HATS-44 (upper right), HATS-45 (lower left), and HATS-46 (lower right). We show models for ages of 0.2 Gyr and 1.0 to 14.0 Gyr in 1.0 Gyr increments (ages increasing from left to right). The adopted values of $T_{\text{eff},*}$ and ρ_* are shown together with their 1σ and 2σ confidence ellipsoids. The initial values of $T_{\text{eff},*}$ and ρ_* from the first ZASPE and light curve analyses are represented with a triangle.

high-precision RV measurements following Pál et al. (2008), Bakos et al. (2010), Hartman et al. (2012).

Photometric light curves are modeled using the Mandel & Agol (2002) models. For HATSouth light curves, we consider the possible over-correction introduced by the trend-filtered algorithm. In the case of the follow-up light curves, systematic trends for each event are corrected by including a time-dependent quadratic signal to the transit model, and a linear signal with up to three parameters describing the shape of the PSF.

Radial velocity data are modeled using Keplerian orbits, where we consider independent zero-points and RV jitter factors for each instrument, which are allowed to vary in the fit. We fitted the four systems by considering two possible cases, the eccentricity as a free parameter, and also by forcing circular orbits. For each system, we estimated the Bayesian evidence of each scenario by using the method presented in Weinberg et al. (2013). We find that for HATS-43, the free-eccentricity model with $e = 0.173 \pm 0.089$ has a significantly higher evidence compared to the model with fixed eccentricity.

For HATS-44 and HATS-45, the Bayesian evidence for the free-eccentricity models are slightly higher than for the fixed circular orbit models; however, in both cases, these results are generated by outlier radial velocity points. For both of these systems, we therefore adopt the fixed circular orbit solutions but note that the eccentricities are poorly constrained by the observations, with 95% confidence upper limits of $e < 0.279$,

and $e < 0.240$, respectively. For HATS-46, we find that the fixed circular orbit model has higher Bayesian evidence, and we adopt the parameters from that model for this system as well. The 95% confidence upper limit on the eccentricity for HATS-46 is $e < 0.559$.

We used a Differential Evolution Markov Chain Monte Carlo procedure to explore the fitness landscape and to determine the posterior distribution of the parameters. The resulting parameters and uncertainties for each system are listed in Table 4 and summarized below.

1. HATS-43b has a Saturn-like mass of $M_p = 0.261 \pm 0.054 M_J$, and a radius of $R_p = 1.180 \pm 0.050 R_J$, which results in relatively low density of $\rho_p = 0.191^{+0.054}_{-0.038} \text{ g cm}^{-3}$. Its orbit is moderately eccentric and due to the low luminosity of its K-type host star, HATS-43b has a rather warm equilibrium temperature of $T_{\text{eq}} = 1003 \pm 27 \text{ K}$. If the fixed circular orbit model is adopted for HATS-43b, the planet presents a somewhat lower mass and density ($0.235 \pm 0.060 M_J$, and $0.164 \pm 0.046 \text{ g cm}^{-3}$, respectively) compared to the adopted model where the eccentricity is allowed to vary.
2. HATS-44b has a sub-Jupiter mass of $M_p = 0.56 \pm 0.11 M_J$, and a radius of $R_p = 1.067^{+0.125}_{-0.071} R_J$, which results in a density of $\rho_p = 0.56 \pm 0.19 \text{ g cm}^{-3}$. Even though the luminosities of HATS-43 and HATS-44 are similar, the

Table 4
Orbital and Planetary Parameters for HATS-43b–HATS-46b

Parameter	HATS-43b Value	HATS-44b Value	HATS-45b Value	HATS-46b Value
Light curve parameters				
P (days)	4.3888497 ± 0.0000059	2.7439004 ± 0.0000032	4.1876244 ± 0.0000056	4.7423729 ± 0.0000049
T_c (BJD) ^a	$2457636.08946 \pm 0.00025$	$2456931.11384 \pm 0.00061$	$2456731.19533 \pm 0.00073$	$2457376.68539 \pm 0.00060$
T_{14} (days) ^a	0.12452 ± 0.00090	0.0688 ± 0.0017	0.1269 ± 0.0021	0.1014 ± 0.0019
$T_{12} = T_{34}$ (days) ^a	0.01666 ± 0.00070	0.029 ± 0.034	0.0207 ± 0.0023	0.0157 ± 0.0017
a/R_*	$13.04^{+0.68}_{-0.41}$	9.24 ± 0.38	9.02 ± 0.39	$13.55^{+0.45}_{-0.65}$
ζ/R_* ^b	18.519 ± 0.075	$42.0^{+3.3}_{-1.7}$	18.65 ± 0.25	23.21 ± 0.28
R_p/R_*	0.1492 ± 0.0017	0.129 ± 0.010	0.1004 ± 0.0042	0.1088 ± 0.0027
b^2	$0.029^{+0.046}_{-0.018}$	$0.743^{+0.051}_{-0.035}$	$0.475^{+0.049}_{-0.060}$	$0.402^{+0.055}_{-0.042}$
$b \equiv a \cos i/R_*$	$0.172^{+0.104}_{-0.066}$	$0.862^{+0.029}_{-0.021}$	$0.689^{+0.034}_{-0.045}$	$0.634^{+0.042}_{-0.034}$
i (deg)	$89.24^{+0.29}_{-0.41}$	84.65 ± 0.38	85.61 ± 0.42	$87.32^{+0.22}_{-0.31}$
HATSouth blend factors ^c				
Blend factor	1.0	1.0	0.810 ± 0.075	$0.877 \pm 0.061, 0.863 \pm 0.068$
Limb-darkening coefficients ^d				
c_1, g	...	0.8140
c_2, g	...	0.0272
c_1, r	0.5115	0.5603	0.2511	0.4078
c_2, r	0.2239	0.1933	0.3818	0.2935
c_1, i	0.3873	0.4195	0.1791	0.3112
c_2, i	0.2588	0.2444	0.3719	0.3042
RV parameters				
K (m s ⁻¹)	37.5 ± 8.0	90 ± 17	75 ± 16	22.1 ± 8.0
e^e	0.173 ± 0.089	<0.279	<0.240	<0.559
ω (deg)	330 ± 120
$\sqrt{e} \cos \omega$	$0.38^{+0.11}_{-0.21}$
$\sqrt{e} \sin \omega$	$-0.141^{+0.130}_{-0.079}$
$e \cos \omega$	$0.159^{+0.092}_{-0.121}$
$e \sin \omega$	$-0.060^{+0.056}_{-0.035}$
RV jitter FEROS (m s ⁻¹) ^f	20.3 ± 7.8	49 ± 11	47 ± 20	32.9 ± 6.7
RV jitter HARPS (m s ⁻¹)	0 ± 10	...	0.0 ± 5.4	...
RV jitter PFS (m s ⁻¹)	22.7 ± 6.8
Planetary parameters				
M_p (M_J)	0.261 ± 0.054	0.56 ± 0.11	0.70 ± 0.15	0.173 ± 0.062
R_p (R_J)	1.180 ± 0.050	$1.067^{+0.125}_{-0.071}$	1.286 ± 0.093	$0.903^{+0.058}_{-0.045}$
$C(M_p, R_p)^g$	-0.01	0.01	0.01	-0.02
ρ_p (g cm ⁻³)	$0.191^{+0.054}_{-0.038}$	0.56 ± 0.19	$0.41^{+0.16}_{-0.11}$	0.28 ± 0.12
$\log g_p$ (cgs)	2.67 ± 0.11	3.08 ± 0.13	3.02 ± 0.12	$2.71^{+0.14}_{-0.20}$
a (au)	0.04944 ± 0.00046	0.03649 ± 0.00030	0.05511 ± 0.00069	0.05367 ± 0.00053
T_{eq} (K)	1003 ± 27	1161 ± 34	1518 ± 45	1054 ± 29
Θ^h	0.0265 ± 0.0057	0.0438 ± 0.0095	0.047 ± 0.011	0.0222 ± 0.0082
$\log_{10} \langle F \rangle$ (cgs) ⁱ	8.359 ± 0.047	8.613 ± 0.051	9.079 ± 0.051	8.445 ± 0.048

Notes. For HATS-43, we adopt a model in which the eccentricity is allowed to vary. For the other three systems, we adopt a model in which the orbit is assumed to be circular. See the discussion in Section 3.3.

^a Times are in Barycentric Julian Date calculated directly from UTC *without* correction for leap seconds. T_c : Reference epoch of mid transit that minimizes the correlation with the orbital period. T_{12} : total transit duration, time between first to last contact; $T_{12} = T_{34}$: ingress/egress time, time between first and second, or third and fourth contact.

^b Reciprocal of the half duration of the transit used as a jump parameter in our MCMC analysis in place of a/R_* . It is related to a/R_* by the expression $\zeta/R_* = a/R_*(2\pi(1 + e \sin \omega))/(P\sqrt{1 - b^2}\sqrt{1 - e^2})$ (Bakos et al. 2010).

^c Scaling factor applied to the model transit that is fit to the HATSouth light curves. This factor accounts for dilution of the transit due to over-filtering of the light curve. These factors are varied in the fit. For HATS-43 and HATS-44, we fix these values to one because the analysis is performed on light curves after applying signal-reconstruction TFA to correct for over-filtering. For HATS-46, we list separately the dilution factors adopted for the G755.2 and G754.3 HATSouth light curves.

^d Values for a quadratic law, adopted from the tabulations by Claret (2004) according to the spectroscopic (ZASPE) parameters listed in Table 3.

^e For fixed circular orbit models, we list the 95% confidence upper limit on the eccentricity determined when $\sqrt{e} \cos \omega$ and $\sqrt{e} \sin \omega$ are allowed to vary in the fit.

^f Term added in quadrature to the formal RV uncertainties for each instrument. This is treated as a free parameter in the fitting routine. In cases where the jitter is consistent with zero, we list its 95% confidence upper limit.

^g Correlation coefficient between the planetary mass M_p and radius R_p estimated from the posterior parameter distribution.

^h The Safronov number is given by $\Theta = \frac{1}{2}(V_{\text{esc}}/V_{\text{orb}})^2 = (a/R_p)(M_p/M_*)$ (see Hansen & Barman 2007).

ⁱ Incoming flux per unit surface area, averaged over the orbit.

smaller semimajor axis of HATS-44b results in a higher equilibrium temperature of $T_{\text{eq}} = 1161 \pm 34$ K.

3. HATS-45b has also a sub-Jupiter mass of $M_p = 0.70 \pm 0.15 M_J$, and an inflated radius of $R_p = 1.286 \pm 0.093 R_J$, which results in a density of $\rho_p = 0.41^{+0.16}_{-0.11} \text{ g cm}^{-3}$. HATS-45b suffers from moderately strong irradiation from its F-type host star, which produces a high equilibrium temperature of $T_{\text{eq}} = 1518 \pm 45$ K.
4. HATS-46b has a mass of $M_p = 0.173 \pm 0.062 M_J$, which lies in the Neptune–Saturn-mass range. We measured a radius of $R_p = 1.286 \pm 0.093 R_J$ for HATS-46b, which combined with the mass gives a density of $\rho_p = 0.28 \pm 0.12 \text{ g cm}^{-3}$. The low luminosity of the host star produces a relatively low equilibrium temperature of $T_{\text{eq}} = 1054 \pm 29$ K for HATS-46b.

3.4. Jitter and Stellar Activity

Our analysis delivers a moderately high jitter value for the four transiting systems. There is no significant evidence of additional planets on them that could explain the increased scatter in the RV residuals. For the case of HATS-43b, a possible explanation for the moderately high jitter can be associated to the activity of the host star. A generalized Lomb–Scargle (GLS) analysis reveals a strong peak at a period of 25 days. The sinusoidal signal in the photometric data associated to that period shows an amplitude of 8 mmag. If this period is assumed as the rotational period of the star, a stellar radius of $0.812 R_\odot$ will produce a rotational velocity of 1.6 km s^{-1} at the surface of the star, which is consistent with the spectroscopically inferred $v \sin i = 1.11 \text{ km s}^{-1}$. The S/N of the spectra is too low for measuring activity indicators in the Ca H and K lines. We also investigated if the stellar activity could be responsible of the high jitter for the other three systems, but we didn't find significant peaks in the GLS analysis. The S/N of the spectra was also too low for measuring activity indicators on them. Another possible explanation for the high jitter of these systems is related to a possible underestimation of the RV error bars. Brahm et al. (2017a) reports a long-term RV precision of $\sim 7 \text{ m s}^{-1}$ for the FEROS based on high S/N spectra of bright stars ($V < 7$). The precision for fainter stars is assumed to follow from the scaling relations presented by Queloz (1995), which depend on the S/N and the width of the cross-correlation peak. However, the host stars of the four systems are moderately faint ($V > 13$), and additional factors that are not taken into account by the empirical scaling relation, like guiding errors or contamination by the simultaneous ThAr lamp, could be responsible for underestimating the RV uncertainties. In the case of the three systems for which additional RVs from other instruments are available, we performed the RV analysis using the data of one spectrograph and then we repeated the analysis using the data of the other one. The orbital parameters that we obtained were consistent between both instruments for the three systems, which validates that the RV variations measured with FEROS are real.

4. Discussion

We have presented the discovery of four new short-period transiting systems from the HATSouth network. The systems

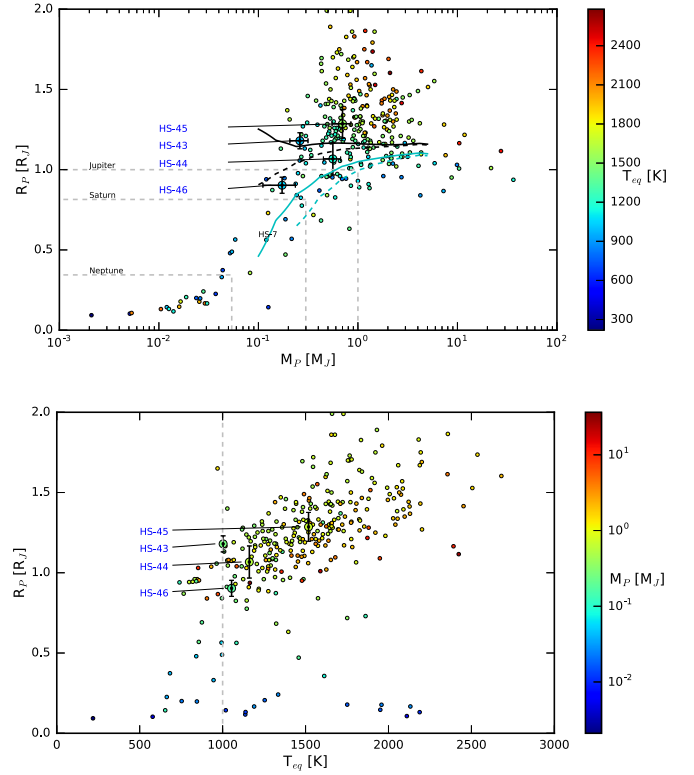


Figure 10. Top panel: planetary mass–radius diagram for the population of well characterized planets with masses and radii measured at the 35% level. The planetary equilibrium temperature is color coded. The big circles with error bars correspond to HATS-43b, HATS-44b, HATS-45b, and HATS-46b. The plotted lines correspond to the Fortney et al. (2007) models for irradiated planets at 0.045 au from the host star. The black lines represent planets with an age of 1 Gyr, while light blue lines represent planet with an age of 4.5 Gyr. From top to bottom, the models contain core masses of 0, 10, 25, and 50 earth masses. Bottom panel: planet radius as a function of the equilibrium temperature for the same systems considered in the upper panel. The dashed gray line corresponds to the temperature limit below which inflation mechanisms of hot Jupiters are not expected to play a major role. While the radii for HATS-44b, HATS-45b, and HATS-46b clearly follow the empirical trend of increasing radius with the insolation level, HATS-43b has a slightly larger radius than the one predicted from this empirical correlation.

were identified as planetary candidates using HATSouth photometric light curves and then confirmed as planetary-mass objects by measuring precise radial velocities for the host stars. The precision of the transit parameters was also improved by using additional follow-up light curves obtained with 1m-class telescopes. We found that the four planets have orbital periods shorter than 5 days and masses in the Neptune to Jupiter mass range, but all of them show radii similar to that of Jupiter.

These four new systems add to the valuable population of extrasolar planets transiting stars with precisely determined masses and radii. In the top panel of Figure 10, we show the planet radius as a function of the planet mass for the population of transiting planets with uncertainties in M_p and R_p at the level of 35%,¹⁹ and we have included our four new systems. The lower panel of Figure 10 uses the same population of planets, but in this case we plot the $T_{\text{eq}}-M_p$ diagram. While both diagrams show that the physical properties of HATS-43b to HATS-46b are consistent with what is expected based on the

¹⁹ Query to exoplanets.eu for systems having reported values of R_* , T_{eff} , $[\text{Fe}/\text{H}]$, and a

Table 5
Discovered Transiting Planets Having Reported M_p and T_{eq} Values Consistent with HATS-43b

Name	$M_p [M_J]$	$T_{\text{eq}} [\text{K}]$	$R_p [R_J]$	$[\text{Fe}/\text{H}] [\text{dex}]$	e	$H [10^{19} \text{ W}]^a$
WASP-29b	0.244 ± 0.020	980 ± 40	$0.792^{+0.056}_{-0.035}$	$+0.11 \pm 0.14$	$0.03^{+0.05}_{-0.03}$	1.18
WASP-69b	0.260 ± 0.017	963 ± 18	1.057 ± 0.047	$+0.15 \pm 0.08$	$<0.1 \text{ at } 2\sigma$	<16
HAT-P-19b	0.292 ± 0.020	1010 ± 42	1.132 ± 0.072	$+0.23 \pm 0.08$	0.067 ± 0.042	14
HATS-5b	0.237 ± 0.012	1025 ± 17	0.912 ± 0.025	$+0.19 \pm 0.08$	0.019 ± 0.019	0.2
HATS-43b	0.261 ± 0.054	1003 ± 27	1.180 ± 0.050	$+0.050 \pm 0.041$	0.173 ± 0.089	52

Note.

^a Tidal heating rate (Jackson et al. 2008).

distribution of known transiting planets, we can point out a few interesting properties.

4.1. HATS-43b

With a mass of $M_p = 0.261 \pm 0.054 M_J$ and an equilibrium temperature of $T_{\text{eq}} = 1003 \pm 27 \text{ K}$ that lies close to the 1000 K limit proposed by Kovács et al. (2010) below which planet radius is not expected to be strongly affected by stellar insolation, this planet has a radius of $R_p = 1.180 \pm 0.050 R_J$, which is particularly large if compared with other systems with similar properties. We can identify four other systems having masses and irradiation levels consistent with the ones of HATS-43b, namely HAT-P-19b (Hartman et al. 2011), WASP-29b (Hellier et al. 2010), WASP-69b (Anderson et al. 2014), and HATS-5b (Zhou et al. 2014). The properties of these systems are summarized in Table 5. HATS-43b has the largest radius of this subsample. Even though the metallicity of HATS-43 is the lowest one, which could hint to the absence of a central solid core and consequently a larger radius, the Fortney et al. (2007) models of planetary structure predict a radius that is more than 2σ below the adopted value for HATS-43b. On the other hand, HATS-43b stands out as the only system of the subsample having an eccentricity greater than 0.1. Given that the physical properties of the stellar hosts of Table 5 are similar, this enhanced eccentricity directly translates in a greater tidal heating rate (Jackson et al. 2008), which could be the driving source responsible for the large radius of HATS-43b.

The low density of HATS-43b makes this system an interesting target for atmospheric studies. Specifically, its expected transmission spectroscopy signal of $\delta_{\text{trans}} = 2350 \text{ ppm}$, is among the highest values from the full population of discovered transiting systems. WASP-39b (Faedi et al. 2011), which has a similar transmission spectroscopy signal ($\delta_{\text{trans}} = 2500 \text{ ppm}$) and similar physical properties to HATS-43b, has been the target of numerous atmospheric studies (Kammer et al. 2015; Fischer et al. 2016; Nikolov et al. 2016) that find that this planet has a cloud free atmosphere with presence of Rayleigh scattering slope and Na and K absorption lines. HATS-43b is a well suited comparison target to study the atmospheres of Saturn-mass planets with even lower temperatures.

4.2. HATS-44b and HATS-45b

HATS-44b with a mass of $M_p = 0.56 \pm 0.11 M_J$ and a radius of $R_p = 1.067^{+0.125}_{-0.071} R_J$, and HATS-45b with a mass of $M_p = 0.70 \pm 0.15 M_J$ and a radius of $R_p = 1.286 \pm 0.093 R_J$ are, two sub-Jupiter mass planets that lie in relatively densely populated regions of the parameter space of transiting systems (see Figure 10). The most similar system to HATS-44b in terms of

planet mass and irradiation level, is WASP-34 ($M_p = 0.59 \pm 0.01 M_J$, $T_{\text{eq}} = 1160 \text{ K}$ Smalley et al. 2011), which has a slightly larger radius of $R_p = 1.22 \pm 0.10 R_J$ which is in agreement with the proposed anti correlation between the planet radius and the metallicity of the host star. WASP-34b has a moderately metal-poor stellar host star ($[\text{Fe}/\text{H}] = -0.02 \pm 0.10$) if compared to HATS-44 ($[\text{Fe}/\text{H}] = +0.32 \pm 0.07$). In the case of HATS-45b, the most similar system is HAT-P-9b ($M_p = 0.78 \pm 0.09 M_J$, $T_{\text{eq}} = 1530 \pm 40 \text{ K}$, Shporer et al. 2009), which presents a significantly inflated radius of $R_p = 1.4 \pm 0.06 R_J$, slightly larger but consistent with the one of HATS-45b.

While the radius of HATS-44b can be predicted by using the Fortney et al. (2007) models invoking a core-less structure, the radius of HATS-45b is larger than predicted, which can be expected due to the moderately high irradiation from its F-type host star, where some of the proposed inflation mechanisms of hot Jupiters might be in play.

Even though both planets have expected transmission signals significantly smaller than HATS-43b ($\delta_{\text{trans}} = 860 \text{ ppm}$ and $\delta_{\text{trans}} = 660 \text{ ppm}$, for HATS-44b and HATS-45b, respectively), there have been previous atmospheric studies of transiting planets with similar values of transmission signal (e.g., Parviainen et al. 2016; von Essen et al. 2017). Additionally, the $v \sin i = 9.90 \pm 0.40 \text{ km s}^{-1}$ of HATS-45 makes of this system and interesting target for the determination of the obliquity through the measurement of the Rossiter–McLaughlin effect. The expected semi-amplitude of the radial velocity anomaly for an aligned orbit is of $K_{\text{RM}} = 30 \text{ m s}^{-1}$.

4.3. HATS-46b

Having a mass of $M_p = 0.173 \pm 0.062 M_J$, HATS-46b lies in the sparsely populated region of the parameter space of transiting systems in the Neptune–Saturn-mass range, which corresponds to the transition zone between ice giants and gas giants. According to the core accretion theory of giant planet formation (Pollack et al. 1996), planetesimals agglomerate to form rocky embryos that, when reaching a threshold mass of $\sim 10 M_{\oplus}$, generate a run away accretion of the surrounding gas of the protoplanetary disk that forms thick H/He dominated envelope (90% in mass). One of the theoretical challenges of this model is to understand how ice giants (like Uranus and Neptune) can avoid the accretion of the massive gaseous envelope. For this reason, the discovery of transiting planets in the ice–gas transition range is important for determining which properties of the systems can play a major role in setting their structure and composition, which can be then linked to different formation models. The large radius of HATS-46b suggests that this planet is probably a low-mass gas giant planet and not a high-mass ice giant. By using the Fortney et al. (2007) models of planetary structure, we find that HATS-46b

Table 6
Relative Radial Velocities and Bisector Spans for HATS-43–HATS-46

BJD (2,450,000+)	RV ^a (m s ⁻¹)	σ_{RV} ^b (m s ⁻¹)	BS (m s ⁻¹)	σ_{BS} (m s ⁻¹)	Phase	Instrument
HATS-43						
7325.68004	-115.0	17.0	0.273	FEROS
7403.66458	16.66	12.00	11.0	16.0	0.042	FEROS
7406.78213	36.66	30.00	-176.0	37.0	0.752	FEROS
7498.50193	-19.51	16.00	-21.0	27.0	0.651	HARPS
7637.79837	-13.01	27.60	-7.0	36.0	0.389	HARPS
7638.81141	29.19	17.50	47.0	23.0	0.620	HARPS
7639.85295	47.39	15.50	-1.0	20.0	0.858	HARPS
7640.83377	0.79	13.80	18.0	18.0	0.081	HARPS
7707.75474	-47.81	20.10	36.0	26.0	0.329	HARPS
7708.70649	10.49	10.20	-19.0	13.0	0.546	HARPS
7714.74483	2.16	15.20	-57.0	21.0	0.922	FEROS
7733.71407	-20.44	10.70	-32.0	15.0	0.244	FEROS
7735.81057	36.66	9.90	-10.0	15.0	0.722	FEROS
7736.55523	37.86	11.80	11.0	16.0	0.891	FEROS
7737.83294	-4.84	11.30	-17.0	16.0	0.182	FEROS
7738.62888	-46.74	11.00	46.0	16.0	0.364	FEROS
7739.67457	-11.04	12.10	-68.0	17.0	0.602	FEROS
7740.55295	46.66	11.40	-64.0	16.0	0.802	FEROS
7742.71078	-83.74	10.70	-15.0	15.0	0.294	FEROS
HATS-44						
7325.65952	74.10	17.00	-12.0	23.0	0.790	FEROS
7328.66737	105.10	25.00	7.0	32.0	0.886	FEROS
7329.69814	-70.90	24.00	-8.0	30.0	0.262	FEROS
7403.68598	6.10	15.00	25.0	19.0	0.226	FEROS
7404.73356	100.10	14.00	-102.0	18.0	0.608	FEROS
7406.58676	-143.90	16.00	-65.0	21.0	0.284	FEROS
7410.60096	70.10	18.00	-199.0	23.0	0.747	FEROS
7714.71960	78.70	20.90	-74.0	28.0	0.581	FEROS
7735.55952	-41.90	14.90	-46.0	19.0	0.176	FEROS
7736.61332	-9.20	14.00	-128.0	19.0	0.560	FEROS
7738.73011	-82.20	14.10	-15.0	19.0	0.331	FEROS
7739.77508	88.70	15.40	-25.0	21.0	0.712	FEROS
7740.78263	-57.60	20.00	227.0	26.0	0.079	FEROS
7741.75344	-147.70	15.30	-10.0	21.0	0.433	FEROS
7742.77786	97.90	14.80	-92.0	20.0	0.807	FEROS
HATS-45						
7030.85122	17.19	33.00	-20.0	14.0	0.557	FEROS
7031.79435	-38.81	27.00	4.0	13.0	0.783	FEROS
7033.76761	-103.81	26.00	33.0	12.0	0.254	FEROS
7036.75613	-19.81	27.00	67.0	13.0	0.967	FEROS
7049.71493	-77.81	28.00	66.0	14.0	0.062	FEROS
7050.79282	-107.81	27.00	23.0	13.0	0.319	FEROS
7053.79937	46.19	31.00	-20.0	14.0	0.037	FEROS
7054.69765	-115.81	60.00	0.252	FEROS
7057.63438	-2.81	24.00	0.953	FEROS
7067.58377	-71.01	35.00	-160.0	26.0	0.329	HARPS
7068.58640	49.99	38.00	66.0	29.0	0.569	HARPS
7069.61845	104.99	36.00	59.0	26.0	0.815	HARPS
7070.57795	-32.01	46.00	127.0	33.0	0.044	HARPS
7071.59384	-81.01	24.00	82.0	17.0	0.287	HARPS
7072.57569	22.99	37.00	99.0	26.0	0.521	HARPS
7403.76988	26.19	27.00	55.0	13.0	0.610	FEROS
7404.79556	-12.81	35.00	49.0	16.0	0.855	FEROS
7447.70623	52.19	31.00	80.0	15.0	0.102	FEROS
HATS-46						
7182.81976	-31.91	14.00	-77.0	19.0	0.121	FEROS
7187.88874	-42.91	14.00	-20.0	19.0	0.189	FEROS
7189.86037	23.09	12.00	6.0	17.0	0.605	FEROS

Table 6
(Continued)

BJD (2,450,000+)	RV ^a (m s ⁻¹)	σ_{RV}^b (m s ⁻¹)	BS (m s ⁻¹)	σ_{BS} (m s ⁻¹)	Phase	Instrument
7192.88690	12.09	14.00	29.0	19.0	0.243	FEROS
7198.91703	10.13	9.89	0.515	PFS
7198.92817	23.52	9.70	0.517	PFS
7199.92164	57.98	9.29	0.727	PFS
7199.93228	31.21	9.31	0.729	PFS
7200.92982	28.89	8.26	0.939	PFS
7200.94141	6.75	12.87	0.942	PFS
7202.90860	0.29	7.76	0.357	PFS
7202.91989	-25.30	10.02	0.359	PFS
7203.90169	-4.99	9.79	0.566	PFS
7203.91219	-37.67	10.21	0.568	PFS
7204.94090	-2.99	7.94	0.785	PFS
7210.89718	13.09	13.00	36.0	17.0	0.041	FEROS
7211.91925	-4.91	12.00	-30.0	16.0	0.257	FEROS
7212.89415	-29.91	11.00	-30.0	15.0	0.462	FEROS
7220.79108	-83.91	14.00	-47.0	19.0	0.127	FEROS
7228.71214	64.09	12.00	16.0	16.0	0.798	FEROS
7230.86819	-7.91	10.00	0.0	13.0	0.252	FEROS
7327.60315	55.09	13.00	-31.0	18.0	0.650	FEROS
7570.88719	-32.91	14.00	38.0	19.0	0.950	FEROS
7576.86278	19.09	13.00	-3.0	18.0	0.210	FEROS
7585.86394	54.49	10.90	22.0	15.0	0.108	FEROS
7591.85299	30.49	14.10	-9.0	16.0	0.371	FEROS
7593.76470	0.89	11.10	-27.0	15.0	0.774	FEROS
7612.69088	27.29	12.20	-29.0	17.0	0.765	FEROS
7614.64079	-45.31	12.80	-17.0	17.0	0.176	FEROS
7647.80684	-26.71	12.10	-3.0	16.0	0.170	FEROS
7727.68958	34.69	12.50	-95.0	17.0	0.014	FEROS

Notes.^a The zero-point of these velocities is arbitrary. An overall offset γ_{rel} fitted independently to the velocities from each instrument has been subtracted.^b Internal errors excluding the component of astrophysical jitter considered in Section 3.3.**Table 7**
Light Curve Data for HATS-43, HATS-44, HATS-45, and HATS-46

Object ^a	BJD ^b (2,400,000+)	Mag ^c	σ_{Mag}	Mag(orig) ^d	Filter	Instrument
HATS-43	56659.57177	-0.02617	0.00629	...	<i>r</i>	HS
HATS-43	56602.51755	-0.00594	0.00565	...	<i>r</i>	HS
HATS-43	56663.96208	-0.01437	0.00523	...	<i>r</i>	HS
HATS-43	56620.07431	0.01737	0.00516	...	<i>r</i>	HS
HATS-43	56716.63096	0.00000	0.00584	...	<i>r</i>	HS
HATS-43	56602.52112	-0.00586	0.00563	...	<i>r</i>	HS
HATS-43	56659.57617	-0.00933	0.00646	...	<i>r</i>	HS
HATS-43	56620.07762	-0.00014	0.00519	...	<i>r</i>	HS
HATS-43	56663.96632	-0.00456	0.00531	...	<i>r</i>	HS
HATS-43	56580.57936	-0.03117	0.00689	...	<i>r</i>	HS

Notes.^a Either HATS-43, HATS-44, HATS-45, or HATS-46.^b Barycentric Julian Date is computed directly from the UTC time without correction for leap seconds.^c The out-of-transit level has been subtracted. For observations made with the HATSouth instruments (identified by “HS” in the “Instrument” column), these magnitudes have been corrected for trends using the EPD and TFA procedures applied *prior* to fitting the transit model. This procedure may lead to an artificial dilution in the transit depths. The blend factors for the HATSouth light curves are listed in Table 4. For observations made with follow-up instruments (anything other than “HS” in the “Instrument” column), the magnitudes have been corrected for a quadratic trend in time, and for variations correlated with up to three PSF shape parameters, fit simultaneously with the transit.^d Raw magnitude values without correction for the quadratic trend in time, or for trends correlated with the seeing. These are only reported for the follow-up observations.




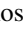
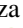











(This table is available in its entirety in machine-readable form.)

should have a core mass of $M_c = 12 \pm 8 M_\oplus$ to explain its mass and radius, implying a $\sim 80\%$ H/He dominated composition. Among the population of discovered transiting systems orbiting main sequence stars with precise mass estimations from RVs, we can identify Kepler-89d ($0.16 M_J$, $0.98 R_J$, Weiss et al. 2013), HATS-8b ($0.14 M_J$, $0.87 R_J$, Bayliss et al. 2015) HAT-P-48b, ($0.17 M_J$, $1.30 R_J$, Bakos et al. 2016), WASP-139b ($0.12 M_J$, $0.80 R_J$, Hellier et al. 2017), and WASP-107b ($0.12 M_J$, $0.94 R_J$, Anderson et al. 2017) as other similar low-mass gas giants, while Kepler-101b ($0.16 M_J$, $0.51 R_J$, Bonomo et al. 2014), HATS-7b ($0.12 M_J$, $0.56 R_J$, Bakos et al. 2015), K2-98b ($0.10 M_J$, $0.38 R_J$, Barragán et al. 2016), and K2-27b ($0.10 M_J$, $0.40 R_J$, Petigura et al. 2017) are compatible with as high-mass ice giants. These two groups of planets can be associated with different locations and/or times of formation. The first group of planets could have been formed relatively close to the host star where the high temperature prevents the formation of icy planetesimals that pollute the planet composition. On the other hand, the second group of planets could have formed farther away or early in the disk lifetime where rocky planetesimals are still present in profusion. This suggested simple classification of these 10 planets is based on the amount of heavy elements inferred from classical models of planetary structure, but there are several additional factors that are not taken into account that can contribute to modify the planetary radius and mislead the determination of the planet metallicity, e.g., evaporation (Owen & Wu 2013), tidal heating (Jackson et al. 2008), or collisions with other planets (Liu et al. 2015). On the other hand, studies of atmospheric composition can be used to directly discriminate if these planets have H/He dominated envelopes or if there is a significant presence of heavier elements, as was recently shown by Wakeford et al. (2017), where a significantly metal depleted composition was estimated for the Neptune mass planet HAT-P-26b. In this context, HATS-46b has a prominent expected transmission signal of ~ 1500 ppm, which should make of this system a valuable target for atmospheric studies. Additional radial velocities for this system will be also valuable for having a more precise estimation of the planetary mass.

Development of the HATSouth project was funded by NSF MRI grant NSF/AST-0723074; operations have been supported by NASA grants NNX09AB29G, NNX12AH91H, and NNX17AB61G, and follow-up observations receive partial support from grant NSF/AST-1108686. J.H. acknowledges support from NASA grant NNX14AE87G. A.J. acknowledges support from FONDECYT project 1171208, BASAL CATA PFB-06, and project IC120009 “Millennium Institute of Astrophysics (MAS)” of the Millennium Science Initiative, Chilean Ministry of Economy. N.E. is supported by BASAL CATA PFB-06. R.B. and N.E. acknowledge support from project IC120009 “Millennium Institute of Astrophysics (MAS)” of the Millennium Science Initiative, Chilean Ministry of Economy. V.S. acknowledges support from BASAL CATA PFB-06. This work is based on observations made with ESO Telescopes at the La Silla Observatory. This paper also uses observations obtained with facilities of the Las Cumbres Observatory Global Telescope. We acknowledge the use of the AAVSO Photometric All-Sky Survey (APASS), funded by the Robert Martin Ayers Sciences Fund, and the SIMBAD database, operated at CDS, Strasbourg, France. Operations at the MPG 2.2 m Telescope are jointly performed by the Max

Planck Gesellschaft and the European Southern Observatory. The imaging system GROND has been built by the high-energy group of MPE in collaboration with the LSW Tautenburg and ESO. We thank the MPG 2.2 m telescope support team for their technical assistance during observations.

ORCID iDs

R. Brahm  <https://orcid.org/0000-0002-9158-7315>
 J. D. Hartman  <https://orcid.org/0000-0001-8732-6166>
 A. Jordán  <https://orcid.org/0000-0002-5389-3944>
 G. Á. Bakos  <https://orcid.org/0000-0001-7204-6727>
 N. Espinoza  <https://orcid.org/0000-0001-9513-1449>
 M. Rabus  <https://orcid.org/0000-0003-2935-7196>
 W. Bhatti  <https://orcid.org/0000-0002-0628-0088>
 K. Penev  <https://orcid.org/0000-0003-4464-1371>
 V. Suc  <https://orcid.org/0000-0001-7070-3842>
 D. Bayliss  <https://orcid.org/0000-0001-6023-1335>
 G. Zhou  <https://orcid.org/0000-0002-4891-3517>
 M. de Val-Borro  <https://orcid.org/0000-0002-0455-9384>
 J. D. Crane  <https://orcid.org/0000-0002-5226-787X>
 P. Arriagada  <https://orcid.org/0000-0002-3578-551X>
 P. Butler  <https://orcid.org/0000-0003-1305-3761>
 B. Schmidt  <https://orcid.org/0000-0002-8538-9195>

References

- Anderson, D. R., Collier Cameron, A., Delrez, L., et al. 2014, *MNRAS*, **445**, 1114
- Anderson, D. R., Collier Cameron, A., Delrez, L., et al. 2017, *A&A*, **604**, A110
- Bakos, G., Noyes, R. W., Kovács, G., et al. 2004, *PASP*, **116**, 266
- Bakos, G. Á., Torres, G., Pál, A., et al. 2010, *ApJ*, **710**, 1724
- Bakos, G. Á., Csabry, Z., Penev, K., et al. 2013, *PASP*, **125**, 154
- Bakos, G. Á., Penev, K., Bayliss, D., et al. 2015, *ApJ*, **813**, 111
- Bakos, G. Á., Hartman, J. D., Torres, G., et al. 2016, arXiv:1606.04556
- Baranne, A., Queloz, D., Mayor, M., et al. 1996, *A&AS*, **119**, 373
- Barragán, O., Grziwa, S., Gandolfi, D., et al. 2016, *AJ*, **152**, 193
- Batygin, K., & Stevenson, D. J. 2010, *ApJL*, **714**, L238
- Bayliss, D., Zhou, G., Penev, K., et al. 2013, *AJ*, **146**, 113
- Bayliss, D., Hartman, J. D., Bakos, G. Á., et al. 2015, *AJ*, **150**, 49
- Bhatti, W., Bakos, G. Á., Hartman, J. D., et al. 2016, arXiv:1607.00322
- Bonomo, A. S., Sozzetti, A., Lovis, C., et al. 2014, *A&A*, **572**, A2
- Brahm, R., Jordán, A., & Espinoza, N. 2017a, *PASP*, **129**, 034002
- Brahm, R., Jordán, A., Hartman, J., & Bakos, G. 2017b, *MNRAS*, **467**, 971
- Brahm, R., Jordán, A., Bakos, G. Á., et al. 2016, *AJ*, **151**, 89
- Brown, T. M., Baliber, N., Bianco, F. B., et al. 2013, *PASP*, **125**, 1031
- Burrows, A., Hubeny, I., Budaj, J., & Hubbard, W. B. 2007, *ApJ*, **661**, 502
- Butler, R. P., Marcy, G. W., Williams, E., et al. 1996, *PASP*, **108**, 500
- Claret, A. 2004, *A&A*, **428**, 1001
- Crane, J. D., Shectman, S. A., Butler, R. P., et al. 2010, *Proc. SPIE*, **7735**, 773553
- Dopita, M., Hart, J., McGregor, P., et al. 2007, *Ap&SS*, **310**, 255
- Espinoza, N., Bayliss, D., Hartman, J. D., et al. 2016, *AJ*, **152**, 108
- Faedi, F., Barros, S. C. C., Anderson, D. R., et al. 2011, *A&A*, **531**, A40
- Fischer, P. D., Knutson, H. A., Sing, D. K., et al. 2016, *ApJ*, **827**, 19
- Fortney, J. J., Marley, M. S., & Barnes, J. W. 2007, *ApJ*, **659**, 1661
- Fraine, J., Deming, D., Benneke, B., et al. 2014, *Natur*, **513**, 526
- Girardi, L., Bressan, A., Bertelli, G., & Chiosi, C. 2000, *A&AS*, **141**, 371
- Hansen, B. M. S., & Barman, T. 2007, *ApJ*, **671**, 861
- Hartman, J. D., Bakos, G. Á., Sato, B., et al. 2011, *ApJ*, **726**, 52
- Hartman, J. D., Bakos, G. Á., Béky, B., et al. 2012, *AJ*, **144**, 139
- Hartman, J. D., Bayliss, D., Brahm, R., et al. 2015, *AJ*, **149**, 166
- Hartman, J. D., Bakos, G. Á., Bhatti, W., et al. 2016, *AJ*, **152**, 182
- Hellier, C., Anderson, D. R., Collier Cameron, A., et al. 2010, *ApJL*, **723**, L60
- Hellier, C., Anderson, D. R., Cameron, A. C., et al. 2017, *MNRAS*, **465**, 3693
- Hippler, S., Bergfors, C., Brandner, W., et al. 2009, *Msngr*, **137**, 14
- Howell, S. B., Sobek, C., Haas, M., et al. 2014, *PASP*, **126**, 398
- Jackson, B., Greenberg, R., & Barnes, R. 2008, *ApJ*, **681**, 1631
- Janson, M., Durkan, S., Hippler, S., et al. 2017, *A&A*, **599**, A70
- Jordán, A., Brahm, R., Bakos, G. Á., et al. 2014, *AJ*, **148**, 29
- Kammer, J. A., Knutson, H. A., Line, M. R., et al. 2015, *ApJ*, **810**, 118

- Kaufer, A., & Pasquini, L. 1998, [Proc. SPIE](#), **3355**, 844
- Kovács, G., Bakos, G., & Noyes, R. W. 2005, [MNRAS](#), **356**, 557
- Kovács, G., Zucker, S., & Mazeh, T. 2002, [A&A](#), **391**, 369
- Kovács, G., Bakos, G. Á., Hartman, J. D., et al. 2010, [ApJ](#), **724**, 866
- Liu, S.-F., Hori, Y., Lin, D. N. C., & Asphaug, E. 2015, [ApJ](#), **812**, 164
- Mandel, K., & Agol, E. 2002, [ApJL](#), **580**, L171
- Mayor, M., Pepe, F., Queloz, D., et al. 2003, [Msngr](#), **114**, 20
- Mordasini, C., Alibert, Y., Georgy, C., et al. 2012, [A&A](#), **547**, A112
- Nikolov, N., Sing, D. K., Gibson, N. P., et al. 2016, [ApJ](#), **832**, 191
- Owen, J. E., & Wu, Y. 2013, [ApJ](#), **775**, 105
- Pál, A., Bakos, G. Á., Torres, G., et al. 2008, [ApJ](#), **680**, 1450
- Parviainen, H., Pallé, E., Nortmann, L., et al. 2016, [A&A](#), **585**, A114
- Penev, K., Bakos, G. Á., Bayliss, D., et al. 2013, [AJ](#), **145**, 5
- Petigura, E. A., Sinukoff, E., Lopez, E. D., et al. 2017, [AJ](#), **153**, 142
- Pollacco, D. L., Skillen, I., Collier Cameron, A., et al. 2006, [PASP](#), **118**, 1407
- Pollack, J. B., Hubickyj, O., Bodenheimer, P., et al. 1996, [Icar](#), **124**, 62
- Queloz, D. 1995, in IAU Symp. 167, New Developments in Array Technology and Applications, ed. A. G. D. Philip, K. A. Janes, & A. R. Upgren (Dordrecht: Kluwer), 221
- Ricker, G. R., Winn, J. N., Vanderspek, R., et al. 2014, [Proc. SPIE](#), **9143**, 914320
- Shporer, A., Bakos, G. Á., Bouchy, F., et al. 2009, [ApJ](#), **690**, 1393
- Smalley, B., Anderson, D. R., Collier Cameron, A., et al. 2011, [A&A](#), **526**, A130
- Sozzetti, A., Torres, G., Charbonneau, D., et al. 2007, [ApJ](#), **664**, 1190
- von Essen, C., Cellone, S., Mallonn, M., et al. 2017, [A&A](#), **603**, A20
- Wakeford, H. R., Sing, D. K., Kataria, T., et al. 2017, [Sci](#), **356**, 628
- Weinberg, M. D., Yoon, I., & Katz, N. 2013, [arXiv:1301.3156](#)
- Weiss, L. M., Marcy, G. W., Rowe, J. F., et al. 2013, [ApJ](#), **768**, 14
- Yi, S., Demarque, P., Kim, Y.-C., et al. 2001, [ApJS](#), **136**, 417
- Zacharias, N., Finch, C. T., Girard, T. M., et al. 2012, [yCat](#), **1322**, 0
- Zhou, G., Bayliss, D., Penev, K., et al. 2014, [AJ](#), **147**, 144
- Zhou, G., Bayliss, D., Hartman, J. D., et al. 2015, [ApJL](#), **814**, L16